Monthly Notices
of the
ROYAL ASTRONOMICAL SOCIETY
MNRAS **475,** 1046–1072 (2018) doi:10.1093/mnras/stx3179

On the nature of hydrogen-rich superluminous supernovae

C. Inserra,[1,2★] S. J. Smartt,[2] E. E. E. Gall,[2,3] G. Leloudas,[4] T-W. Chen,[5] S. Schulze,[6,7] A. Jerkstrand,[8] M. Nicholl,[9] J. P. Anderson,[10] I. Arcavi,[11,12†] S. Benetti,[13] R. A. Cartier,[1] M. Childress,[1] M. Della Valle,[14] H. Flewelling,[15] M. Fraser,[16] A. Gal-Yam,[17] C. P. Gutiérrez,[1] G. Hosseinzadeh,[11,12] D. A. Howell,[11,12] M. Huber,[15] E. Kankare,[2] T. Krühler,[5] E. A. Magnier,[15] K. Maguire,[1] C. McCully,[11,12] S. Prajs,[1] N. Primak,[15] R. Scalzo,[18,19] B. P. Schmidt,[20] M. Smith,[1] K. W. Smith,[2] B. E. Tucker,[18,19] S. Valenti,[21] M. Wilman,[15] D. R. Young[2] and F. Yuan[18,19]

Affiliations are listed at the end of the paper

Accepted 2017 December 4. Received 2017 December 1; in original form 2017 September 29

ABSTRACT

We present two hydrogen-rich superluminous supernovae (SLSNe): SN2103hx and PS15br. These objects, together with SN2008es, are the only SLSNe showing a distinct, broad H α feature during the photospheric phase; also, they show no sign of strong interaction between fast moving ejecta and circumstellar shells in their early spectra. Despite the fact that the peak luminosity of PS15br is fainter than that of the other two objects, the spectrophotometric evolution is similar to SN2103hx and different from any other supernova in a similar luminosity space. We group all of them as SLSNe II and hence they are distinct from the known class of SLSN IIn. Both transients show a strong, multicomponent H α emission after 200 d past maximum, which we interpret as an indication of the interaction of the ejecta with an asymmetric, clumpy circumstellar material. The spectra and photometric evolution of the two objects are similar to Type II supernovae, although they have much higher luminosity and evolve on slower time-scales. This is qualitatively similar to how SLSNe I compare with normal type Ic, in that the former are brighter and evolve more slowly. We apply a magnetar and an interaction semi-analytical code to fit the light curves of our two objects and SN2008es. The overall observational data set would tend to favour the magnetar, or central engine, model as the source of the peak luminosity, although the clear signature of late-time interaction indicates that interaction can play a role in the luminosity evolution of SLSNe II at some phases.

Key words: circumstellar matter – stars: magnetars – supernovae: general – supernovae: individual: SN2103hx – supernovae: individual: PS15br – supernovae: individual: SN2008es.

1 INTRODUCTION

Over the past few years, the current generation of wide-field optical surveys has discovered a new class of intrinsically bright transients, which show absolute magnitudes at maximum light of $M_{\rm AB} \sim -21$ mag, total radiated energies of order 10^{51} erg (e.g. Quimby et al. 2011). These are now commonly called superluminous supernovae (SLSNe; Gal-Yam 2012). They are factors of 5–100 brighter than Type Ia or normal core-collapse SNe and they have recently been classified on their spectrophotometric behaviour rather than a simple magnitude threshold (e.g. Papadopoulos et al. 2015; Lunnan et al. 2016; Prajs et al. 2017).

Two distinct groups have emerged so far. The first, and best studied, includes hydrogen-free SLSNe, which have spectra at maximum light showing a blue continuum and a distinctive W-shaped spectra feature in absorption at ∼4200 Å. The absorption has been identified as O II and these SNe have been labelled SLSNe I (Quimby et al. 2011; Gal-Yam 2012). Their spectra at about 30 d after peak are very similar to normal or broad-lined SNe Ic at peak luminosity (Pastorello et al. 2010), and hence are also called SLSNe Ic (Inserra et al. 2013b).

The second group is that of hydrogen-rich SLSNe. This includes the very bright, strongly interacting SNe such as SN2006gy (e.g. Smith et al. 2007; Smith & McCray 2007; Ofek et al. 2007;

★E-mail: c.inserra@soton.ac.uk
†Einstein fellow.

Table 1. Main properties of the SLSNe II presented here.

	SN2103hx	PS15br
Alternative names	SMTJ013533283–5757506	CSS150226–112519+081418 MLS150612–112519+081418
α (J2000.0)	$01^h35^m32\overset{s}{.}83$	$11^h25^m19\overset{s}{.}22$
δ (J2000.0)	$-57°57'50\overset{''}{.}6$	$8°14'18\overset{''}{.}9$
z	0.125	0.101
Peak g (mag)	−21.70	−20.22
$E(B-V)$ (mag)	0.02	0.06
L_{ugriz} peak ($\times 10^{43}$ erg s^{-1})	10.78	2.43
Light-curve peak (MJD)	56684.50 ± 1.00	57089.25 ± 2.00
Host r (mag)	−15.58(A), −14.81(B)	−16.25

Agnoletto et al. 2009). The enormous luminosity of these is mainly powered by the interaction of supernova ejecta with dense circumstellar (CSM) shells and thus, following the standard taxonomy, they should be labelled SLSNe IIn (due to the clear hydrogen multicomponent and narrow emission lines exhibited since the early spectra).

However, there is also one known SLSN that, in many ways, is similar to SLSNe Ic, but with a distinct and broad Hα feature. This is SN2008es, which has been studied by Miller et al. (2009) and Gezari et al. (2009) and does not obviously show any signs of interaction between fast and slow moving ejecta and CSM shells. The favoured explanation for this object, which resembled a normal luminosity SN II (Miller et al. 2009), was a core-collapse explosion of a non-standard progenitor star with a super wind and extended envelope (Gezari et al. 2009). Recent papers have also shown SLSNe I with weak, but distinct, multicomponent Hα emission (Benetti et al. 2014) or with late-time Hα emission (Yan et al. 2015, 2017).

It is plausible that there are multiple powering sources in any of these explosions. For example, a central engine may power the bulk of the luminosity, but then interaction between the magnetar powered ejecta and some CSM shells (of varying density) could provide additional energy output and alter the spectra morphology as observed for a nearby sample of slow SLSNe I (Inserra et al. 2017c). Hereafter, we will refer to events without obvious spectral signatures of interaction as SLSNe II, whereas those with narrow spectral features, multicomponent profiles and obviously powered by interaction will be referred to as SLSNe IIn. In this paper, we present two more SLSNe II objects, followed in detail by the Public ESO Spectroscopic Survey for Transient Objects (PESSTO; Smartt et al. 2015) with $H_0 = 72$ km s^{-1}, $\Omega_M = 0.27$ and $\Omega_\lambda = 0.73$ adopted as standard cosmology.

2 SAMPLE

2.1 SN2103hx

SN2103hx (SMTJ013533283–5757506) was discovered by the SkyMapper Transient (SMT) and Supernova Survey (Keller et al. 2007; Scalzo et al. 2013) on the 2013 December 27 in g and r bands. Three weeks before the discovery, on MJD 56632.55, an image from the SMT shows no detection of the transient to $r \simeq 20.28$ mag. Hence, we can determine the epoch of explosion to around 20 d, at least as far as the sensitivity of the images allows. The object coordinates have been measured on our astrometrically calibrated images: $\alpha = 01^h35^m32\overset{s}{.}83 \pm 0\overset{s}{.}05$, $\delta = -57°57'50\overset{''}{.}6 \pm 0\overset{''}{.}05$ (J2000). The object brightened slowly by ∼1 mag in the observed g band from discovery to peak. The photometry is given in Table C1. It was classified by PESSTO (Smartt et al. 2015) around maximum as a hydrogen-rich superluminous supernova showing some similarities to SN2010gx (Pastorello et al. 2010) and CSS121015:004244+132827 (Benetti et al. 2014) on February 20 UT (Campbell et al. 2014; Scalzo et al. 2014b). The spectrum showed a blue continuum with broad features in the blue together with a narrow emission feature at ∼7500 Å consistent with Hα setting the object at $z = 0.125$ (see Table 1 for the main properties of SN2103hx). It was then immediately selected by PESSTO as a follow-up science target and a combination of optical, near-infrared (NIR) and ultraviolet (UV) photometric monitoring, together with optical spectroscopic monitoring, was carried out (see a summary in Table 2). Observations and data reduction are reported in Appendix A. The Galactic reddening towards the position of the SN is $E(B-V) = 0.02$ mag (Schlafly & Finkbeiner 2011). The available spectra do not show Na ID lines from the host galaxy, and hence we adopt the Galactic reddening as total reddening.

Deep gri images taken by PESSTO with the New Technology Telescope (NTT) + EFOSC2 on the 2015 December 10, after the SN faded, find an extended, faint source at $\alpha = 01^h35^m32\overset{s}{.}78 \pm 0\overset{s}{.}05$, $\delta = -57°57'52\overset{''}{.}3 \pm 0\overset{''}{.}05$ (J2000), which is at 2 arcsec from the SN's location (4.36 kpc at $z = 0.125$). The magnitudes of this galaxy are $g = 24.43 \pm 0.16$, $r = 23.20 \pm 0.16$ and $i = 21.82 \pm 0.16$ mag (Host A). This source was not detected in the NIR with deep J, H, K images taken by PESSTO with the NTT + SOFI on 2015 December 17 ($J > 23.1$ mag; see Table C1 for the limits in each filter). Even deeper images from Magellan + IMACS on 2016 February 1 showed faint flux closer to the location of SN2013hx (within 0.″5) at magnitude $g = 24.71 \pm 0.38$, $r = 24.55 \pm 0.35$ and $i = 23.54 \pm 0.32$ mag (Host B). This flux could either be the true host or residual flux from SN2013hx or a combination of both. Given that the Magellan detections are close to 3σ significance and that star/galaxy separation is not reliable at these flux limits, we avoid any conclusion on the true host (but see Schulze et al. 2018, for an in-depth analysis).

2.2 PS15br

PS15br was discovered by the Pan-STARRS Survey for Transients (PSST; Huber et al. 2015)[1] on 2015 February 16 at $w_{P1} = 19.10 \pm 0.02$ mag, confirmed as a transient source the day after and subsequently detected by the Catalina Real-time Transient Survey (CRTS; Drake et al. 2009, with IDs CSS150226–112519+081418 and MLS150612–112519+081418) at $R = 18.3$ mag on 2015 February 26. The closest pre-detection image is on 2015 January 16 from CRTS images. We measured

[1] http://star.pst.qub.ac.uk/ps1threepi/psdb/

Table 2. Observations log (see Appendix A for further information).

Type	Phase	Observations
	SN2103hx	
Photometry	early/photospheric (≤110d)	Skymapper; NTT+EFOSC2; Swift+UVOT; LCO+Sinestro
	late/nebular(>110d)	NTT+EFOSC2; NTT+SOFI
Spectroscopy	early/photospheric (≤110d)	NTT+EFOSC2; ANU+WiFeS
	late/nebular (>110d)	NTT+EFOSC2; VLT+FORS2
	PS15br	
Photometry	early/photospheric (≤110d)	LCO+Sinestro; LT+IO:O; PSST; CSS; Swift+UVOT; NTT+SOFI
	late/nebular(>110d)	NTT+EFOSC2; LT+IO:O; NTT+SOFI
Polarimetry	early/photospheric (≤110d)	VLT+FORS2
Spectroscopy	early/photospheric (≤110d)	NTT+EFOSC2; ANU+WiFeS; UH+SNIFS
	late/nebular (>110d)	NTT+EFOSC2; VLT+XHOOTER

the object's coordinates on our astrometrically calibrated images: $\alpha = 11^{h}25^{m}19\overset{s}{.}22 \pm 0\overset{s}{.}05$, $\delta = 8^{\circ}14'18\overset{''}{.}9 \pm 0\overset{''}{.}05$ (J2000). The SN was observed to rise slowly with these multiple detections by PSST and CRTS and was then classified by PESSTO on 2015 March 11 (Fraser et al. 2015) as a superluminous supernova around maximum light at $z = 0.101$ (see Table 1 for PS15br's main properties). As for the previous target, PS15br was also followed up by the PESSTO consortium and monitored with optical + UV + NIR imaging and optical + NIR (only at late-time) spectroscopy, which revealed the presence of Balmer lines. A summary of PS15br observations can be found in Table 2. Because of the additional spectroscopy presented here, we were able to secure the classification as SLSN II. The foreground reddening is $E(B - V) = 0.06$ mag from Schlafly & Finkbeiner (2011). Also, in this case, the available spectra do not show Na ID lines from the host galaxy and we only adopt the Galactic reddening.

We retrieved stacks from the Pan-STARRS1 Science Consortium 3π survey (Tonry et al. 2012; Schlafly et al. 2012; Magnier et al. 2013) with total exposure times of *g* (720s), *r* (590s), *i* (1800s), *z* (930s) from before the explosion of PS15br, which are unlikely to contain SN flux (see Table C2 in Appendix C). Aperture photometry produced the following AB magnitudes for the extended host galaxy $g_{P1} = 22.39 \pm 0.11$, $r_{P1} = 22.18 \pm 0.12$, $i_{P1} = 21.70 \pm 0.09$ and $z_{P1} = 22.15 \pm 0.11$ mag. We estimate that the centre of this dwarf host galaxy is 0.6 arcsec from the SN's location (which would be 1 kpc at $z = 0.101$) and within the uncertainties this is effectively coincident. The photometric measurements of the host are in agreement with the Sloan magnitudes of the galaxy SDSS J112519.21+081417.9 listed in the Sloan Digital Sky Survey (SDSS) Data Release 12 (Alam et al. 2015).

3 PHOTOMETRIC, SPECTROSCOPIC AND POLARIMETRIC EVOLUTION

3.1 Light curves

SN2103hx shows a light curve with a 30-d rise in the observer frame in both *g* and *r* bands (see the left panel of Fig. 1), reaching an absolute peak magnitude of −21.70 in the rest-frame *g* band. A relatively close non-detection and a low-order polynomial fit point towards to a rise time of 40 ± 10 d (∼37d in the rest frame) from the explosion. The rest-frame decline in the *g* band is 2.0 mag $100d^{-1}$ (phase < 10 d), while in the *V* band it is 4.5 mag $100d^{-1}$ (phase > 20 d), suggesting a linear decline similar to that of SN2008es showing 2.9 mag $100d^{-1}$ in the *g* band. This would imply that SLSNe II fall on the right/top part of the $s2/M_{max}$[2] distribution of SNe II Anderson et al. (2014a) and broadly follow the trend ($s2_{SLSNeII} \gtrsim$ 2.9 mag and M_{max}(SLSNeII) > −19 mag). This would support an association between SLSNe II and normal SNe II. The untimely end of our observational campaign in 2013 March was due to the right ascension of the object.[3] The second season started when it reappeared again in July and PESSTO restarted its annual observing periods in 2013 August. Hence, the follow-up campaign recovered SN2103hx some five months after maximum light in this second season. From 160 d after peak, the light curves show a steady decline in all bands.

PS15br was detected during the rise phase, only in the *w* band of PSST and by the Catalina Sky Survey (CSS). We continued to observe the SN until it disappeared behind the Sun in 2015 July and started again in 2015 December. We fit the data with a low-order polynomial and find the peak epoch consistent with MJD 57089.25 ± 2.00. Then, the non-detection of the transient 30 d before the first detection suggests a rise time of ∼35 d in the rest frame, and hence similar to that of SN2103hx (see right panel of Fig. 1 where *w*-band measurements have been converted in the *r* band through SNAP; see Appendix B). However, the rest-frame peak magnitudes of −20.22 (*g*) and <−20.75 (*U*) are fainter than those of SN2103hx and SN2008es while the spectroscopic evolution is similar to theirs (see also Sections 3.2 and 5). PS15br shows a fairly rapid and linear decline in the UV and *u* bands after peak, which is gradually less steep in the redder bands. In *B*, *V*, *g* and *r* bands, the light curves show a slower second decline with 1.2 mag $100d^{-1}$ in the *g* band between 30 and 90 d post-peak in the rest frame. The last two photospheric epochs of PS15br could suggest a faster decrease similar to that experienced by some SNe II at a similar phase (see Valenti et al. 2015), which could correspond to the end of hydrogen recombination. In the second season (phase >250 d) the light curves show a very slow, almost flat, behaviour in all bands. This is the consequence of interaction between the SN ejecta and CSM material similar to that experienced by SN2103hx (see Section 5).

Because of PS15br's fainter peak luminosity with respect to the other two objects, it is important to understand how it compares with the few hydrogen-rich SNe populating a similar absolute luminosity space. PS15br shows an overall slower evolution than

[2] We have used the s2 parameter as we do not observe a transition from cooling to recombination phase, usually measured with the s1 parameter.
[3] Some of these data, mainly an early version of the rest-frame *g* band and bolometric light curve, were previously given to Nicholl et al. (2015) as a courtesy.

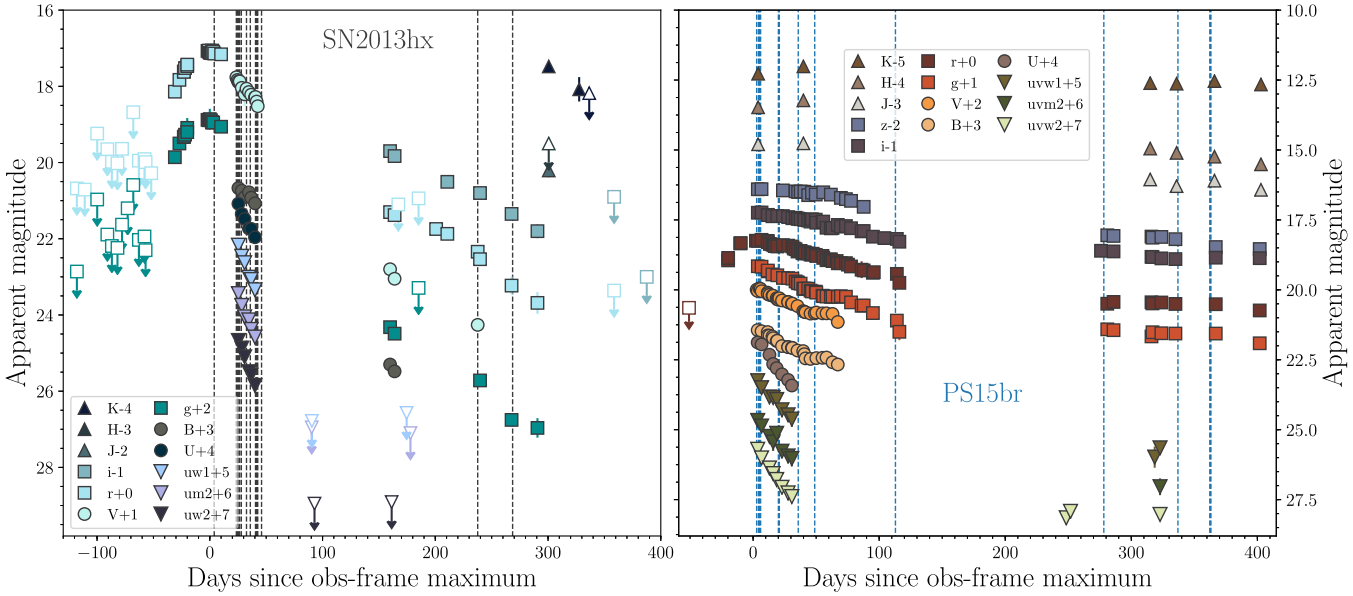

Figure 1. Left: *uvw*2, *uvm*2, *uvw*1, *U*, *B*, *V*, *g*, *r*, *i*, *J*, *H*, *K* light-curve evolution of SN2103hx in the observed frame. Right: *uvw*2, *uvm*2, *uvw*1, *U*, *B*, *V*, *g*, *r*, *i*, *z*, *J*, *H*, *K* light-curve evolution of PS15br in the observed frame. Open symbols denote limits. Phase is with respect to maximum light at observed frame in the *r* band. Uncertainties are also reported The epochs of SN2103hx and PS15br spectra are marked with black and blue vertical dashed lines, respectively.

other objects at similar absolute magnitude ($\gtrsim -19.5$ in the *g* band; Arcavi et al. 2016), suggesting that PS15br is different from the transients showing peak magnitude between those of normal SNe II and SLSNe. The only other non-SLSN object displaying a similar brightness is the SN IIn/IIL SN2013fc ($M_g \sim -20.2$; Kangas et al. 2016), which decreases by >3.1 mag $100\,d^{-1}$ in the *g* band in the first 90 d. Moreover, SN2013fc displays a similar spectroscopic behaviour to SNe II, suggesting a CSM interaction as the source for its bright peak luminosity. Although PS15br's peak luminosity is closer to the range between SLSN and normal SNe II, it shows a photometric behaviour and spectroscopic evolution different from the objects presented in Arcavi et al. (2016) and Kangas et al. (2016).

3.2 Spectroscopy

The spectra evolution of the two SNe is shown in Fig. 2 (see Table C7). Both SN2103hx (left panel of Fig. 2) and PS15br (right panel of Fig. 2), like SN2008es (Gezari et al. 2009; Miller et al. 2009), show no typical broad absorption features of O II that we see in SLSNe I. We note that the spectra have temperatures consistent with the photospheric temperatures at which these ionic transitions are prominent (12 000–16 000 K; Quimby et al. 2013; Inserra et al. 2013b), even though such ions could be sensitive to non-thermal radiation in a way similar to He I (Mazzali et al. 2016). In general, the post-peak spectra of both objects show Balmer lines, He, Ca, Fe and other metal lines.

The first spectrum of SN2103hx, 3 d after peak, shows a broad H α and He I λ5876, while that of 21 d past peak also shows conspicuous Balmer lines and an emission feature at ∼4600 Å similar to those observed in PS15br and SN2008es (see Fig. 3). This feature was also present in the first spectrum but weaker. The emission peak of this feature could again be associated with C III/N III, possibly even contaminated by Fe III forest lines rather than He II λ4686 (see Fig. 3). All the Balmer lines have a P Cygni profile with the exception of H α showing only the emission component up to ∼30 d after peak. However, the absorption component exhibited by H α in the +36 to +38 d spectra is weak. Such behaviour resembles that of fast-declining SNe II (or SNe IIL). A transient unresolved narrow H α line tentatively detected in our first spectrum may point towards some weak interaction at early times; however, such behaviour is seen in many SNe II at early times (e.g. Fassia et al. 2001; Gal-Yam et al. 2007; Inserra et al. 2013a; Gutiérrez et al. 2017a). A shallow He I λ5876 line, possibly blended with Na ID, is visible until 40 d after maximum. The Ca H&K lines are visible from +20.8 d, as well as a feature in absorption at ∼5000 Å likely related to the Fe II multiplet $\lambda\lambda$4924, 5018, 5169. Two other P Cygni profiles are visible from 20 to 40 d after peak at 3745 and 4575 Å, which, based on the similarities with SNe II, we identify as Fe I. They are possibly blended with Ti II, and Fe II, respectively.

An absorption feature is visible from +23 d to +38 d in SN2103hx (and less clearly from +5 d to +19 d in PS15br) on the blue side of H α with an absorption minimum at 6250 Å. This absorption feature has been observed in several SNe II (Chugai, Chevalier & Utrobin 2007; Inserra et al. 2011, 2012a; Inserra, Baron & Turatto 2012b; Inserra et al. 2013a; Valenti et al. 2014, 2015; Bose et al. 2015) at both early or late photospheric epoch, and it is called 'cachito' (Gutiérrez et al. 2017a). The two interpretations are high-velocity hydrogen originating from the interaction between rapidly expanding SN ejecta and a CSM or Si II λ6355. The latter seems the most plausible identification in our objects as it shows a velocity consistent with, although slightly lower than, other metal lines such as Fe II (see Section 4.4).

In the earliest spectrum of PS15br there is a feature at 4600 Å that could be associated with C III/N III rather than He II λ4686 (see Fig. 3). This feature already weakens in the spectrum at 5 d after maximum and has been observed in several non-SLSNe II (e.g. SNe 1998S, 2007pk, 2009bw, 2013cu; Fassia et al. 2001; Inserra et al. 2012a, 2013a; Gal-Yam et al. 2014). PS15br never shows a broad H α absorption component but displays a multicomponent emission profile due to the combination of a relatively broad feature ($v \sim 1500$ km s^{-1}) and a narrow component ($v \sim 110$ km s^{-1}). This is likely due to the host galaxy as it has a similar width to those of the [O III] emission lines of the host galaxy at λ4959 ($v \sim 110$ km s^{-1}) and λ5007 ($v \sim 100$ km s^{-1}) as measured from our WiFeS

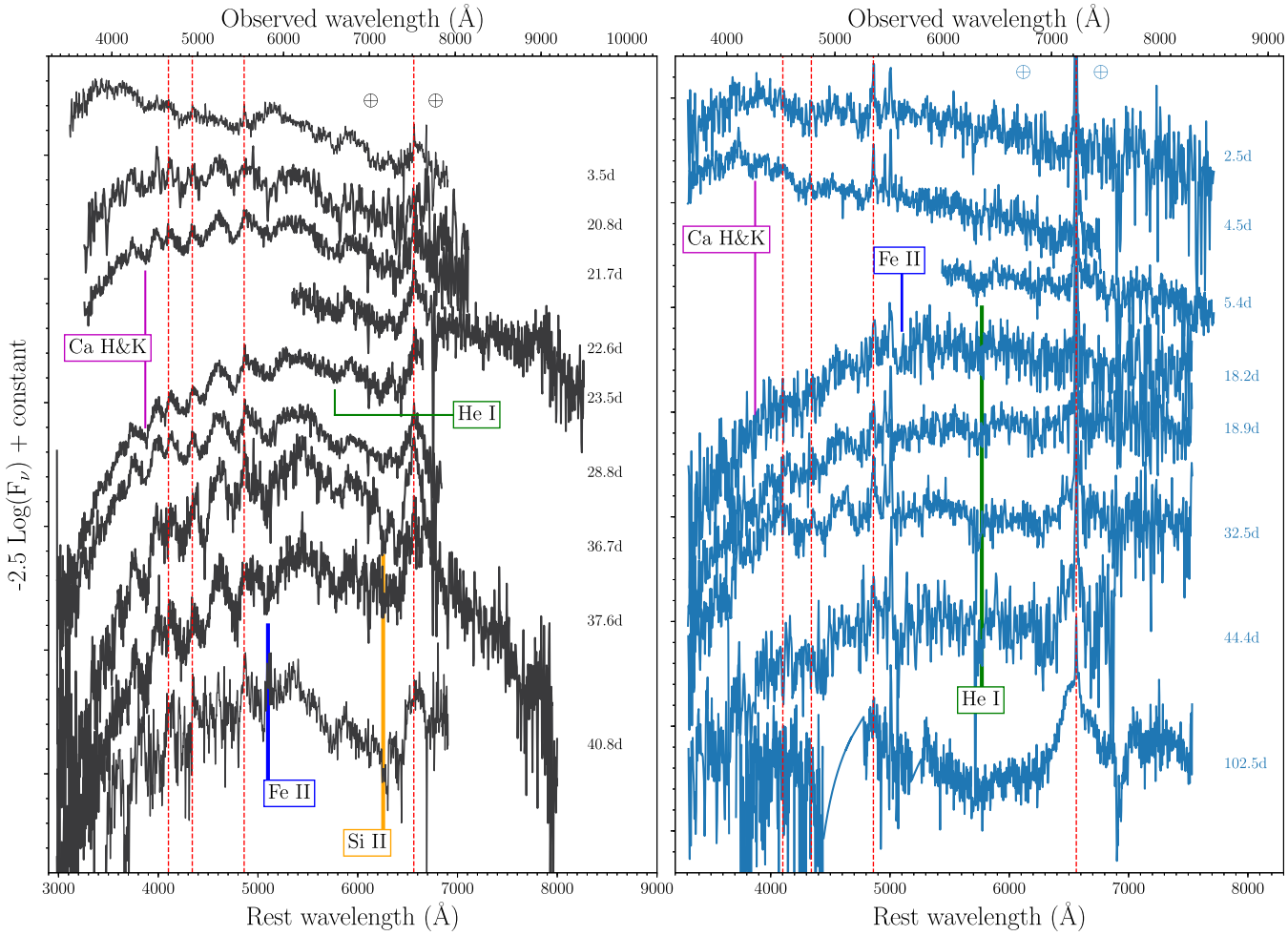

Figure 2. Left: selection of photospheric spectra evolution of SN2103hx. Right: selection of spectra evolution of PS15br. The phase of each spectrum relative to light-curve peak in the rest frame is shown on the right. The spectra are corrected for Galactic extinction and reported in the rest frames. The most prominent features are labelled. Balmer lines H α to H δ are marked with red vertical dashed lines. The $\oplus$ symbols mark the positions of the strongest telluric absorptions. WiFeS spectra were convolved with a factor of 5 and subsequently binned to a 5-Å scale.

spectrum at early time (+4d) and Xshooter spectra at late time (337 and 362 d after maximum). This highlights that there is no evolution in the strength of the line and it supports their identification as a galaxy line because they are comparable to those of the host galaxies of SLSNe in previous studies (e.g. Leloudas et al. 2015a). H β has a similar behaviour although the absorption component is visible from 20 d after maximum. Ca II H&K is visible in the first spectrum and becomes more prominent from day 18 when the metal lines appear, as shown by the presence of the Fe II multiplet $\lambda\lambda$4924, 5018, 5169 and possibly Fe I that replaces the 4600-Å feature. He I λ5876, or a combination of this element with Na ID $\lambda\lambda$5890, 5896, is detectable in the first spectrum and clearly from the third, showing a P Cygni profile.

The last three PS15br spectra of the photospheric phase (32–102 d) show the appearance of a broad component – full width at half-maximum (FWHM) $\sim$ 8000 km s^{-1} – at H α, which is strongly asymmetric in the final photospheric spectrum at 102 d (see Fig. 2). The centroid of the broad H α feature is obscured by the narrow galactic emission line, but is certainly blueshifted and we estimate its peak is at $-$750 km s^{-1}. The asymmetric blue emission is common for H α of SNe II and could be due to an opaque core concealing the outermost layers of the receding part of the envelope where the H α is formed (Chugai 1985). Alternatively, it might be the result of a steep density profile of the hydrogen layer, which increases the probability to observe blueshifted photons because the opacity is mainly due to electron scattering and the line emission mostly comes from the region below the continuum photosphere (Dessart & Hillier 2005; Anderson et al. 2014b).

Considering the slower light-curve decline of PS15br compared to SN2103hx and SN2008es, the formation of the early PS15br H α profile is likely to be related to a weak interaction occurring at early epochs, whereas the SN ejecta would be responsible for the profile of late epochs. PS15br is not a textbook interacting supernova as other ions, such as Fe II and Ca H&K, are observed with a P Cygni profile during its photospheric evolution. The spectrophotometric early behaviour suggests an interaction with a nearby dense circumstellar medium that is swept up in the first week after maximum light. This behaviour is observed in many SNe II (Yaron et al. 2017; Morozova, Piro & Valenti 2017; Moriya et al. 2017), which show a transition from spectra with signs of weak interactions at early time to typical SNe II later (14–30 d after the explosion). Combining such spectroscopic evidence with the slow light-curve decline, we suggest that PS15br is a more luminous version of a transitional SN II, but still different with respect to luminous SNe IIn (e.g. Smith et al. 2007) showing a distinct spectrphotometric evolution.

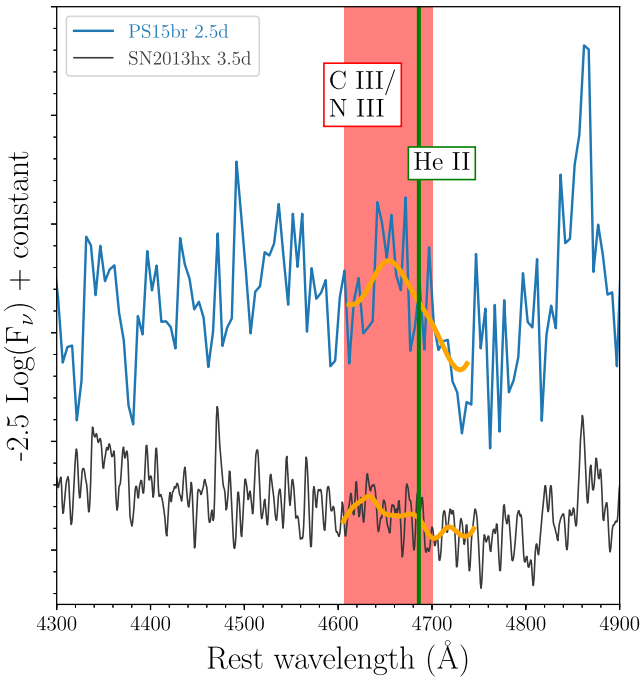

Figure 3. First spectrum of each SN in the region around 4600 Å with the rest-frame He II λ4686 marked by a green vertical line and the region of C III/N III lines by a red area. A Gaussian filter (in orange) has been applied to highlight the wavelength region of interest.

The spectral evolution of these objects is similar (in the observed ions and their strength) and provides additional information about hydrogen-rich SLSNe.

3.3 Imaging polarimetry

On 2015 March 14 UT 05.2, corresponding to a rest-frame phase of 6 d after maximum, we obtained broad-band polarimetry of PS15br with the FORS2 instrument of the Very Large Telescope (VLT) using the *V* filter.[4] We observed it in four different half-wave retarder plate angles: 0, 22.5, 45 and 67.5 deg. The exposure time was 150 s for each angle. The data were reduced in a standard manner by using bias and flat frames, without polarization units in the light path. We obtained point spread function (PSF) photometry of PS15br and six field stars in the field of view (FOV) and we determined their Stokes parameters. The measurements were corrected for instrumental polarization (Patat & Romaniello 2006) and interstellar polarization (ISP). For more details on the reductions and analysis, see Leloudas et al. (2015b).

Fig. 4 shows the location of PS15br and the field stars on the *Q*–*U* plane, after correcting for instrumental polarization. The error bars that are shown are the measurement errors resulting from the PSF fitting and essentially depend on the signal-to-noise (S/N) ratio (∼500 for PS15br). The field stars (light green and red points) present a significant scatter in this plane and the SN signal (purple) is comparable to that of the field stars. Therefore, it is likely that the signal of the field stars and the SN is dominated by ISP. Patat & Romaniello (2006) showed that the instrumental-induced

[4] Unfortunately only one epoch was obtained due to a combination of decreasing apparent magnitude and ending of the European Southern Observatory (ESO) semester.

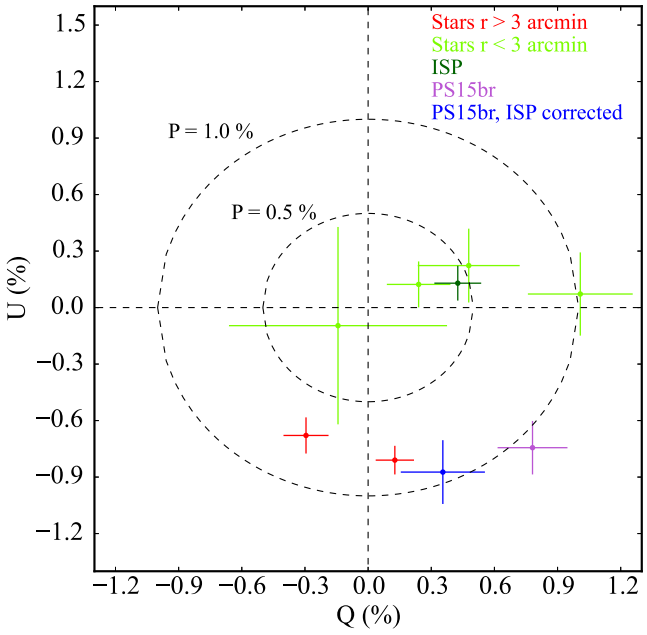

Figure 4. *Q*–*U* plane of PS15br at +6 d from maximum light. Concentric circles show polarization degrees of 0.5 and 1.0 per cent.

polarization in FORS1 – an instrument with an identical design to that of FORS2 – has a radial pattern with polarization increasing as we move away from the optical axis. The two field stars that are the main cause of the scatter (red) are at the outskirts of the FOV, more than 3.6 arcmin from PS15br, which is in the centre of the FOV. However, the measurements of the stars closer to the object (light green) are self-consistent with each other and can be used for a more accurate determination of the ISP.

The ISP is shown in Fig. 4 as the weighted average of the light-green stars. Therefore, despite the fact that all points have been corrected for instrumental polarization – using the FORS1 relation in Patat & Romaniello (2006) – it is possible to obtain a self-consistent picture by only using field stars closer to the optical axis and the SN. These result in a consistent determination of the ISP ($Q_{\rm ISP} = 0.42 \pm 0.11$ per cent and $U_{\rm ISP} = 0.13 \pm 0.09$ per cent), and are clearly different from the properties of PS15br ($Q_{\rm SN} = 0.78 \pm 0.17$ per cent and $U_{\rm SN} = -0.74 \pm 0.14$ per cent).

By correcting for the ISP so evaluated, we obtain a significant polarization signal $Q = 0.36 \pm 0.20$ per cent and $U = -0.87 \pm 0.17$ per cent, resulting in $P = 0.94 \pm 0.17$ per cent. After correcting for polarization bias, according to Patat & Romaniello (2006), this value reduces to $P_0 = 0.93 \pm 0.17$ per cent. Thus, this level of polarization would correspond to an asymmetry of $E \sim 10$–15 per cent, assuming an ellipsoidal photosphere (Hoflich 1991). Such a level of polarization is consistent with that reported for SLSN I SN2015bn at similar epochs (Inserra et al. 2016b; Leloudas et al. 2017) but higher than that of SLSN I LSQ14mo (Leloudas et al. 2015b), for which no evidence for significant deviation from spherical symmetry was found. However, such measurements are higher than those reported for SNe II soon after peak (see Wang & Wheeler 2008, for a review) and a factor of 2 less than that of SNe IIn (e.g. SN1998S; Wang et al. 2001), which are dominated by strong H emission lines not visible in PS15br.

However, as we assume that all field stars are equally good for the determination of the ISP, we conclude that there is a significant scatter – probably pointing to an unaccounted source of systematic

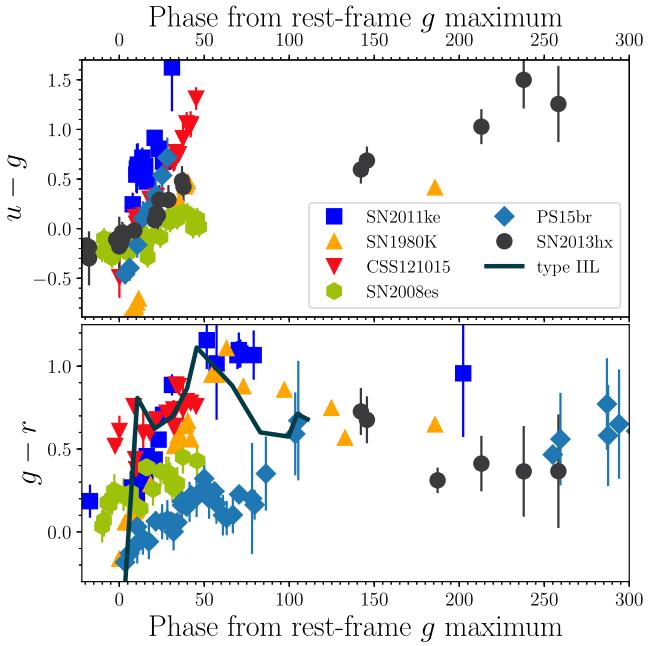

Figure 5. Comparison of the dereddened and *K*-corrected colour evolutions. SN2103hx and PS15br are shown, together with SLSN II SN2008es (Gezari et al. 2009; Miller et al. 2009), SLSNe I SN20011ke (Inserra et al. 2013b) and CSS121015 (Benetti et al. 2014), and SN II SN1980K, for which the colour curve is actually $U - B$ (top panel) and $B - V$ (bottom panel). We also show an SN IIL template from Sanders et al. (2015).

error – and that no conclusive evidence on the source of the polarization associated with PS15br can be derived. Unfortunately, there are no other suitable stars (bright and not saturated) in the FOV of PS15br to resolve this uncertainty.

4 PUTTING TYPE II SUPERLUMINOUS SUPERNOVAE INTO CONTEXT

4.1 Colour curves

As colour curves are useful probes of the temperature evolution of SNe, we computed the rest-frame curves, after accounting for the reddening and redshift effects of time-dilation and *K*-correction. In Fig. 5, SN2103hx and SN2008es show a constant $u - g$ increase towards redder values. However, PS15br is ∼0.25 mag bluer than other SLSNe II at peak. Its colour evolution is also steep, but similar to the prototypical SLSNe I SN2011ke and CSS121015, a SLSN I showing early interaction with a H-shell. This could support the suggestion of an early, weak interaction in PS15br, as observed in several transitional SNe II. We also note that after 20 d, the $u - g$ colour evolution gradient of SN2103hx is similar to that of fast-declining SNE II (or SNe IIL, $u - g \sim 0.4$ mag), whereas PS15br is slightly steeper and SN2008es slightly shallower. Although the former is, overall, shifted redwards.

SLSNe II (PS15br and SN2008es) $g - r$ colours show a similar behaviour with a slow, monotonic increase towards redder colours until 50 d. SLSNe II do not show the constant colour exhibited by SLSNe I from the pre-peak phase to ∼15 d (Inserra et al. 2013b). In general, the colours evolve more slowly to the red than SNe IIL, which cool down to $g - r \sim 0.6$ in the first 20 d, as shown by a template colour evolution (Sanders et al. 2015). We note that although such a template is derived from SNe II, the peak luminosity and light-curve evolution of the objects are similar to SNe IIL, as in other sample papers using Bessell filters (e.g. Li et al. 2011; Faran et al. 2014; Galbany et al. 2016; Valenti et al. 2016). In addition, it appears that PS15br $g - r$ shows a turnover at 50 d and evolves bluewards before turning to the red again. However, considering the uncertainties and comparing the colour curve with the temperature behaviour (see Section 4.4), there might be a flattening in the colour evolution (at $g - r \sim 0.24$ mag) rather than a blueward evolution. The object then clearly evolves to the red afterwards and with $g - r = 0.6$ mag after 100 d it appears similar to SN2103hx and SNe II. After 200 d, SN2103hx and PS15br colour curves remain steady at $g - r = 0.4$ mag and $g - r = 0.6$ mag in a similar fashion to that experienced by normal SNe II/IIL such as SN1980K.

4.2 Bolometric luminosity

UV to NIR photometry is required to obtain a direct measurement of the full bolometric luminosity. This is typically difficult to achieve at all epochs during a SN evolution. Despite the lack of data, valid corrections can be applied to the observed photometric bands to compute the total bolometric flux (see Pastorello et al. 2015; Chen et al. 2015; Kangas et al. 2016; Inserra et al. 2017c, for further insight).

The effective temperatures of the photosphere of SLSNe II during their first 30–50 d after explosion are between $T_{bb} \sim 10\,000$ and 16 000 K (see Section 4.4). This means that their fluxes peak in the UV ($\lambda < 3000$ Å) during this period while our rest-frame *ugri* bands typically cover from 3500 Å redwards. Thus, a significant fraction of the flux is not covered by the optical *ugri* imaging, as testified by the UV to total luminosity ratio for SN2008es and PS15br (see the middle panel of Fig. 6). At around 20 d after peak, the effective temperatures tend to drop below 10 000 K, and hence the spectral energy distributions (SEDs) peak between 3000 and 4000 Å. Although the peak of the SED moves redward, a significant amount of the bolometric flux is radiated in the UV even during these late stages. In the following, we use the term 'pseudo-bolometric light curve' to refer to a bolometric light curve determined using only the optical filters with the flux set to zero outside the observed bands.

To calculate the bolometric luminosity, the broad-band magnitudes in the available optical bands were converted into fluxes at the effective filter wavelengths, and then were corrected for the adopted extinctions (see Section 2). A SED was then computed over the wavelengths covered and the flux under the SED was integrated, assuming there was zero flux beyond the integration limits. Fluxes were then converted to luminosities using the distances previously adopted. We initially determined the points on the pseudo-bolometric light curves at epochs when *ugri* were available simultaneously (or very close in time) and later for epochs with coverage in less than the four filters. Magnitudes from the missing bands were generally estimated by interpolating the light curves using low-order polynomials ($n \leq 3$) between the nearest points in time. For some points, this interpolation was not possible and hence we extrapolated the magnitudes, assuming constant colours from neighbouring epochs.

Becaue SN2103hx and SN2008es have similar optical light curves, we built the SN2103hx bolometric light curve considering the same NIR flux contribution of SN2008es at early epochs (SN2008es broad-band data were retrieved by Miller et al. 2009; Gezari et al. 2009). To check the validity of this assumption, we also estimated the bolometric light curve, integrating, from UV to NIR wavelengths (1000–25 000 Å), our best blackbody fit to the

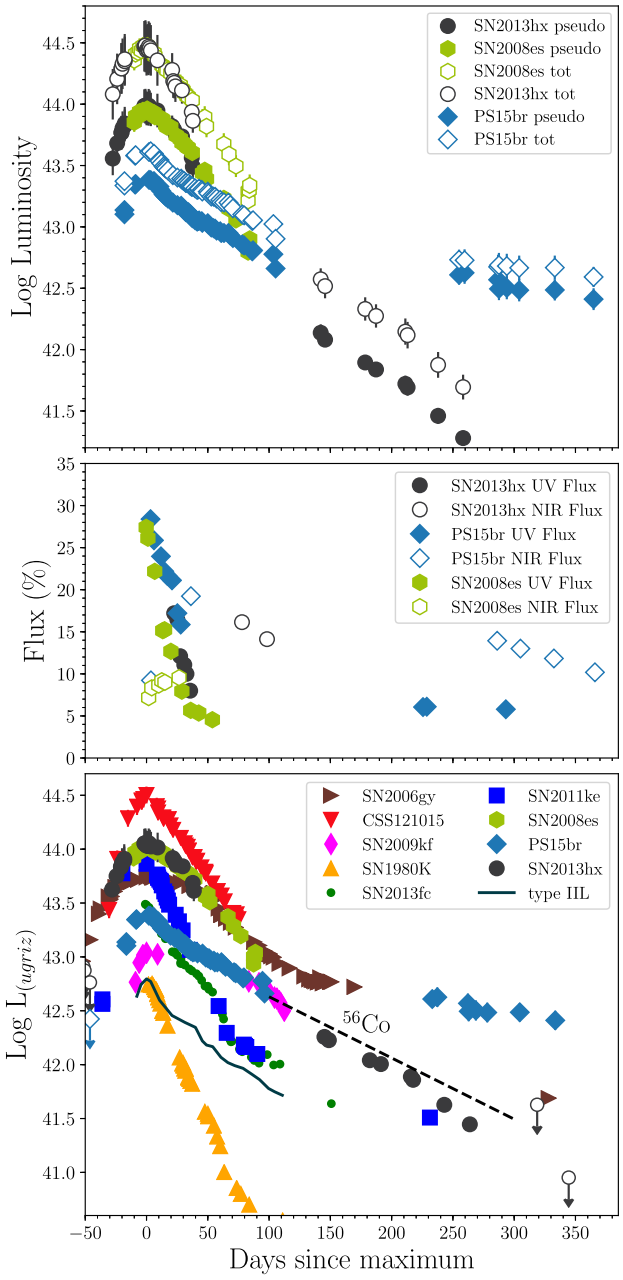

Figure 6. Top: pseudo-bolometric light curves (filled symbols) and proper bolometric light curves (open symbols) of the three SLSNe II. Middle: percentage of the bolometric flux in UV (filled symbols) and NIR (open symbols) with respect to the total bolometric flux derived from data of SLSNe II. Bottom: comparison of pseudo-bolometric light curves (*ugriz*) of SN2103hx, PS15br and SLSN II 2008es (Gezari et al. 2009; Miller et al. 2009), the interacting SLSN IIn 2006gy (Smith et al. 2007), the prototypical SLSN I SN2011ke (Inserra et al. 2013b) and the early interacting SLSN I CSS121015 (Benetti et al. 2014), the SNe II 1980K (Barbon, Ciatti & Rosino 1982) and 2009kf (Botticella et al. 2010), the bright and mild interacting SN II 2013fc (Kangas et al. 2016), as well as an SN IIL template (Sanders et al. 2015). These bolometric light curves are computed after correcting the observed broad-band photometry for time dilation and applying *K*-corrections, through SNAKE (see Appendix B), and extrapolating up to the *z* band when this was unavailable. The black dashed line is the slope of ^{56}Co to ^{56}Fe decay.

available SN2103hx SED. We found similar NIR flux contribution to the bolometric light curve to that of the previous method. The difference between these two methods is included as uncertainty in the evaluation of the SN2103hx bolometric light curve. In Fig. 6 (middle panel), we compare UV and NIR contributions to the total bolometric luminosity of SN2103hx and PS15br with that of SN2008es. The UV contributions are similar and drop almost to zero after 60 d from maximum, while the NIR contribution increases with time. We have late NIR data in *JHK* information for SN2103hx and PS15br, whereas SN2008es only has data in the *J* and *H* bands at these epochs where the NIR contribution becomes significant. If we were to ignore the PS15br *K*-band contribution, the two percentages of NIR contribution (*JH* of PS15br and SN2008es) are similar. Therefore, when we evaluated the full bolometric light curves of SN2103hx and SN2008es, we added the *K*-band contribution estimated specifically by PS15br NIR data.

The peak luminosities of our bolometric light curves are $L_{\rm SN2103hx} \approx 2.75 \times 10^{44}$ erg s^{-1}, $L_{\rm PS15br} \approx 4.15 \times 10^{43}$ erg s^{-1} and $L_{\rm SN2008es} \approx 3.00 \times 10^{44}$ erg s^{-1}, while the maximum luminosities reached by the pseudo-bolometric light curves are almost factor of 2 lower. We note that SN2008es values are in agreement with those previously reported by Gezari et al. (2009); Miller et al. (2009).

The bottom panel of Fig. 6 compares the pseudo-bolometric light curves *ugriz* of our sample of SLSNe II (i.e. SN2103hx, SN2008es and PS15br) with that of the peculiar SLSN I CSS121015, a prototypical SLSN I (SN2011ke) and SNe II. We note that the extrapolation up to the *z* band has been done assuming constant colour from neighbouring epochs or integrating the best-fitting blackbody to the available SED up to the *z*-band coverage. The comparison shows that light curves of SN2103hx and SN2008es are notably similar. CSS121015 also exhibits a fairly similar decline over the first 40 d, but is 0.5 dex brighter than any other SN. The SN2103hx rise appears slower than typical SLSN I events such as SN2011ke. PS15br is ∼0.5 dex fainter than the other two SLSNe II and sits in the gap between normal luminosity SNe II and SLSNe II. Although PS15br exhibits a similar decline to SN2008es and SN2103hx over the first 30 d, it clearly does not show the faster decline observed after this epoch – it remains on a linear decline for nearly 100 d. During this time baseline, it also shows a similar overall decline rate similar to that of one of the brightest SNe II, SN2009kf (Botticella et al. 2010). PS15br is slower than the interacting SN2013fc (Kangas et al. 2016), which is the only SN II reaching a luminosity similar to those of PS15br due to its early interaction. The PS15br decline of ∼0.4 dex over the first 40 d after peak is similar to that shown by the SN IIL template on a similar time-scale, but slower afterwards.

The comparison shows that both SN2103hx and SN2008es have fairly similar shaped profiles within 10–20 d of peak. To make quantitative comparisons of the light-curve widths, we measured a width when the pseudo-bolometric flux is $1/e$ less than that at maximum light in order to match the estimates of the diffusion time-scale parameter τ_m in Nicholl et al. (2015). When these epochs were not specifically covered by a data point, we initially used low-order polynomial fits ($n \leq 4$) to interpolate and find the width (see Fig. 7). The values are reported in Table 3. We note that the values are slightly different than those reported in Nicholl et al. (2015), which could be the result of a small difference in the evaluation of the bolometric light curves. The uncertainties reported are estimated from the differences between the values achieved with different polynomial orders and time baselines. We also employed Gaussian processes (GP), which are generic supervised learning methods widely used in the machine learning community (Bishop 2006;

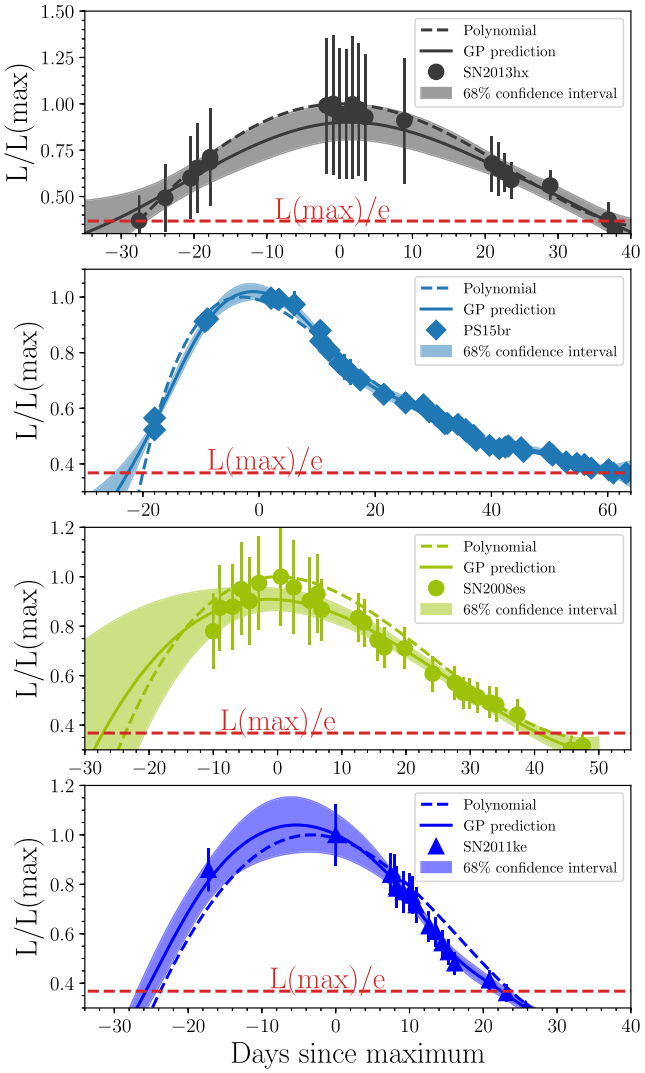

Figure 7. Pseudo-bolometric light curves (*ugriz*) normalized to the maximum of the data, which is at 0 d. The luminosity equivalent to $L(\max)/e$ is highlighted by a red dashed line. We note that the GP peak for SN2008es and SN2011ke occurs earlier in time than that of the polynomial and data.

Rasmussen & Williams 2006) for Bayesian regression and classification problems and are used successfully in the context of SN (e.g. Kim et al. 2013; Scalzo et al. 2014a; de Jaeger et al. 2017) and SLSN light-curve fitting (Inserra et al. 2017a). An important advantage of GP regression compared to other regression techniques is that it produces a best-fitting model, together with uncertainty at each point and a full covariance estimate of the result at unknown points (Ivezic et al. 2014). We used the machine learning packages GEORGE (Ambikasaran et al. 2015) written in PYTHON and a Matern 3/2 kernel to fit our light-curve width (see Inserra et al. 2017a, for further details about the methodology, the kernel and package choice). The results are reported in Table 3, while a comparison with the polynomial fitting can be seen in Fig. 7. Because the two methods seem to be comparable overall, hereafter we refer to the GP results and not to those of the polynomial fitting.

As highlighted before, the decline of SLSNe II tends to be slower than that of SLSNe I such as SN2011ke (a prototypical SLSN I), while the rise time is comparable for all objects. The $1/e$ width is $\gtrsim$70 d for SLSNe II and around 50 d for SN2011ke. We used the same techniques to measure the width of CSS121015 (SLSN I interacting with a hydrogen shell) and found it to be similar to that of SN2011ke. This is a consequence of the sharp rise and decline from peak luminosity observed in the bottom panel of Fig. 6. We also note that SN2103hx and SN2008es have a similar decline from 20 to 50 d. The width of the main peak in PS15br is also not comparable to that of the SLSN IIn SN2006gy (Smith et al. 2007), as the latter has a much wider light curve of ∼110 d (see the bottom panel of Fig. 6). Furthermore, the PS15br peak is strongly asymmetric (see Figs 6 and 7 and Table 3), a detail that is evidence against a strong interaction with a hydrogen-rich massive shell typical of SNe IIn (and SLSN IIn), which would have resulted in a wide, almost symmetric light-curve peak. The slower decline experienced by PS15br is comparable to that of the bright SN II SN2009kf and could be the consequence of a more massive hydrogen layer – and hence higher contribution from hydrogen recombination – than those of the other SLSNe II. Alternatively it could be due to interaction in a similar manner to what has been observed in weakly or mildly interacting SNe II, such as SNe 2007pk (Pritchard et al. 2012; Inserra et al. 2013a), PTF11iqb (Smith et al. 2015) and 2013fc (Kangas et al. 2016). These SNe can be explained by an interaction, weaker than that of SNe IIn, with a dense CSM most likely caused by wind acceleration (Morozova et al. 2017; Moriya et al. 2017), which affects spectra and light-curve evolution in a less dramatic way than observed in SNe IIn/SLSNe IIn such as SN2006gy.

4.3 Spectroscopic resemblance to other SLSNe and SNe II

In the top panel of Fig. 8, the comparison of the spectra around +20 d post maximum with those of the other SLSNe such as SN2008es, SN2011ke and CSS121015 highlights a difference in the line evolution between SLSNe II and both a prototypical (SN2011ke) and peculiar (CSS121015) SLSN I. CSS121015 shows weaker H than SN2013hx and SN2008es with an equivalent width (EW) $\mathrm{EW(H}\alpha)_{\mathrm{SN2013hx,\ SN2008es}} \sim 10 \times \mathrm{EW(H}\alpha)_{\mathrm{CSS121015}}$. CSS121015 also exhibits Fe II lines, which are more prominent than the SLSNe II at a similar phase. Indeed, the Fe absorption lines in CSS121015 are stronger than those of SLSNe II SN2103hx, PS15br and SN2008es with $\mathrm{EW(Fe)}_{\mathrm{CSS121015}} \approx \mathrm{EW(Fe)}_{\mathrm{SLSNeI}} \sim 5\text{–}10 \times \mathrm{EW(Fe)}_{\mathrm{SLSNeII}}$. Both SN2103hx and PS15br are also different from typical SLSNe I spectra. These show the same metal lines observed in CSS121015

Table 3. Width of SLSNe pseudo-bolometric *ugriz* light curves. P refers to the polynomial measurements, while GP denotes those performed with Gaussian processes.

SN	Width (P) (d)	Rise (P) (d)	Decline (P) (d)	Width (GP) (d)	Rise (GP) (d)	Decline (GP) (d)
SN2103hx	64 ± 3	27	37	69 ± 8	31 ± 7	38 ± 4
PS15br	80 ± 5	20	60	83 ± 4	23 ± 4	60 ± 4
SN2008es	67 ± 5	24	43	70 ± 16	30 ± 16	40 ± 4
SN2011ke	48 ± 3	24	24	47 ± 4	18 ± 3	29 ± 2

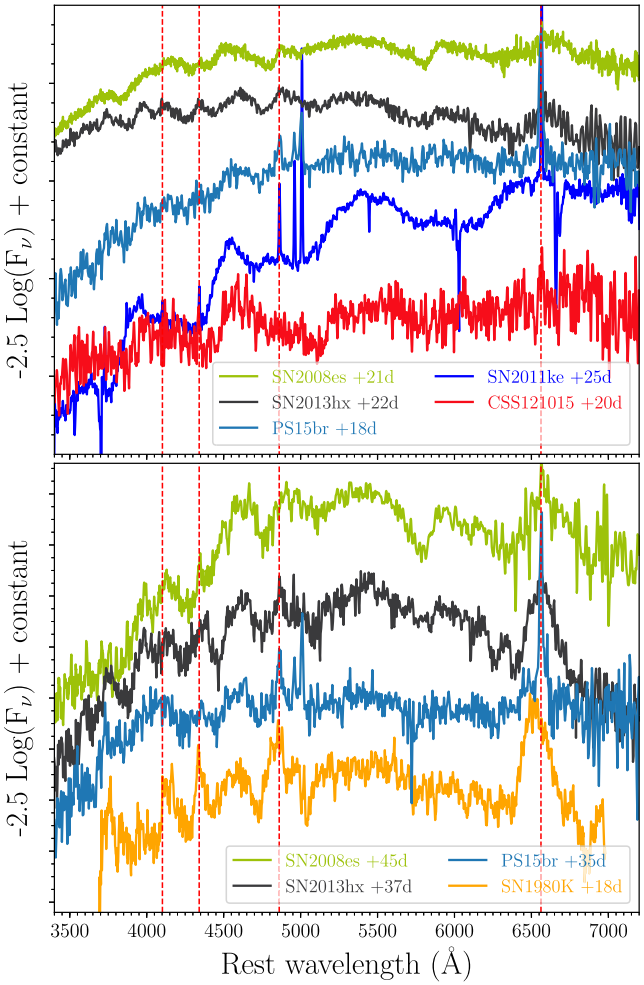

Figure 8. Top: comparison in Log(F$_\nu$) space, which highlights spectral features of SN2103hx and PS15br spectra at ∼20 d from maximum with those of SLSNe showing hydrogen in their spectra, i.e. SN2008es (Miller et al. 2009) and CSS121015 (Benetti et al. 2014), together with SLSN I SN2011ke (Inserra et al. 2013b). Bottom: comparison of the spectra of SN2103hx and PS15br at ∼40 d from maximum together with that of SN2008es at a similar epoch and that of the SN II, SN1980K, at ∼20 d after maximum light. The spectra of the three SLSNe II are similar to those of SNe II in a similar fashion to SLSNe I at ∼30 d resembling SN Ic at maximum. H α to H δ are marked with red vertical dashed lines in all panels.

at similar epochs. The difference between SLSNe I, dominated by broad metal lines, and SLSNe II (SN2008es, SN2103hx, PS15br), exhibiting H lines with weaker metal lines with respect to the SLSNe I, is highlighted in the top panel of Fig. 8. To investigate if SLSNe II spectroscopically behave in a similar fashion to what is observed for SLSNe I (Pastorello et al. 2010; Inserra et al. 2013b) in Fig. 8 (bottom panel), we compare the spectra of SN2103hx and PS15br with that of SN2008es at around 40 d, together with that of the SN II, SN 1980K[5] at 20 d past maximum light. There is an overall resemblance between SLSNe II and SN1980K. At these epochs, SNe II/IIL exhibit $v \sim 8200$ km s^{-1} components in H α while SN2103hx shows $v \sim 8000$ km s^{-1}. Similar trends are visible for H β, with v(H β)$_{\rm SN1980K} \sim 7900$ km s^{-1}, which is similar to v(H β)$_{\rm SN2013hx} \sim 7000$ km s^{-1}. In addition, the strength of the He I λ5876 line is similar between the objects (EW$_{\rm SN1980K} = 10$ Å compared to EW$_{\rm SN2013hx} = 11$ Å, while EW$_{\rm SN2008es} = 18$ Å). This also holds true for the Fe II feature, which has EW$_{\rm SN1980K} = 16$ Å and EW$_{\rm SN2013hx} = 18$ Å. Blueward of H β, the profiles begin to differ, mainly due to Fe I/Ti II shown around 4000 Å in SLSNe and a stronger Ca H&K (EW$_{\rm SLSNeII} \sim 2$–$3 \times$ EW$_{\rm SN1980K}$). The line profiles of PS15br are similar to those of SN2103hx and SN2008es, with the only exception being the H α profile, which does not show an absorption component, and a weak He I. This supports the theory that a certain degree of weak/mild interaction is at play in PS15br. PS15br does not show a blue pseudo-continuum, which would result in a rise of the flux bluewards from ∼5400 Å (e.g. Turatto et al. 2000; Benetti et al. 2014; Inserra et al. 2016a), which characterizes certain types of SN IIn spectra or the blue spectra with only Lorentian Balmer emission-lines typical of SLSNe IIn, such as SN2006gy (Smith et al. 2007). Indeed, bluewards from H α, PS15br is similar to SN2103hx and SN2008es in line strength.

[5] Some of such spectra were digitalized and flux calibrated in Benetti (1992).

4.4 Velocity and temperature evolution

In the left panel of Fig. 9, the evolution of the temperature is plotted in logarithmic space. It is derived from the blackbody fit to the continuum of our rest-frame spectra (big symbols) and colour temperatures (small symbols). Only SN2103hx has multiband coverage before peak allowing us to estimate the temperature pre-peak (17 000–15 000 K; ∼ 4.2 dex). SN2103hx shows a monotonic decline from 14 000 K (4.15 dex) at peak to 6600 K (3.82 dex) at 40 d, while PS15br declines from 12 000 K (4.08 dex) to 6000 K (3.78 dex) showing similar temperatures to SN2103hx and SN2008es in the same time coverage. After 50 d, the temperatures of the objects flatten at ∼5500 K (3.74 dex). SN2008es shows a similar temperature evolution to that of SN2103hx. The overall temperature evolution of SN2103hx, PS15br and SN2008es is similar to that observed in SLSNe I and normal SNe II with a similar decline to those of SNe II. We note that in the first 10 d after maximum, PS15br shows a drop in temperature similar to those of SNe II and SN2103hx, but ∼0.1 dex fainter than the latter.

In the right panel of Fig. 9, the expansion velocities for our SLSNe, as inferred from the position of the absorption minima of the P Cygni profiles for H α and Fe II (average of $\lambda\lambda$4924, 5018, 5169), are compared with those of the only other SLSN II SN2008es, an average of SLSNe I and SNe II. The uncertainties were estimated from the scatter between several measurements. In the case of H α, the velocities were computed from the FWHM of the emission lines for PS15br and for SN2008es in spectra after 40 d. H α velocities decline monotonically from 12 000 to 7500 km s^{-1} on the time-scale available for SN2103hx. An almost identical decrease is observed in SN2008es and PS15br in the available period, 20 < phase (d) < 45, even if PS15br values are due to the broad emission component. The decline rate is qualitatively similar to normal luminosity SNe II, which have average velocities that are lower by about 1200 km s^{-1} at similar epochs, whereas SN1980K H α velocity evolution resembles those of SLSNe II. The velocities measured from the FWHM of the emission components appear to be systematically higher than those inferred from the minima. The Fe II velocities are usually assumed to be better tracers of the photospheric velocity and they are similar in SN2013hx, SN2008es and PS15br, decreasing from 6000 to 4000 km s^{-1} (we note that our measurements are in agreement with those presented by Nicholl et al. 2015). These show the same decline as displayed in normal faster-declining SNe II, but with a shift or delay of ∼15–20 d. SLSNe II Fe II velocities are

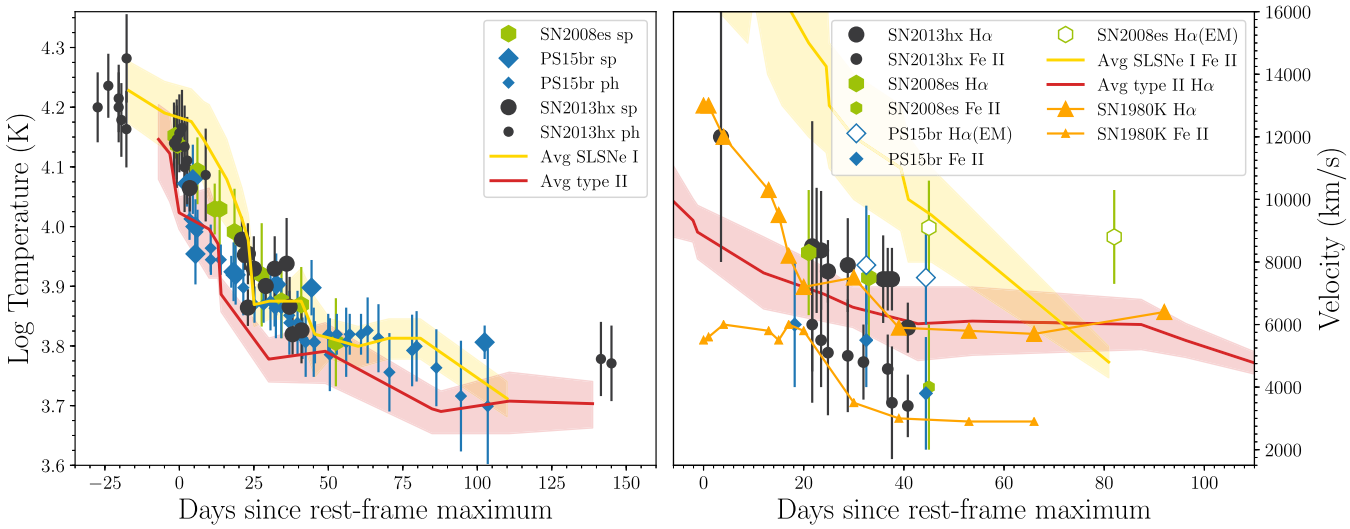

Figure 9. Left: SN2103hx (black) and PS15br (blue) temperature evolution compared with that of SN2008es (green). The gold region represent the 99.73 per cent region of the temperature space of SLSNe I (Inserra et al. 2013b; Nicholl et al. 2015), while the red denotes a Type II collection (Elmhamdi et al. 2003; Maguire et al. 2010; Inserra et al. 2011, 2012a; Botticella et al. 2010; Tomasella et al. 2013; Gutiérrez et al. 2017b). Right: H α and Fe II evolution of SN2103hx (black) and PS15br (blue) compared with that of SN2008es (green), the Type II SN1980K (orange triangle and line for H α and smaller symbols for Fe II; Barbon et al. 1982). The gold region represents the velocity space of Fe II line in SLSNe I, while the red is that of H α in SNe II. Open symbols refer to velocities computed with the FWHM of the emission lines.

different from those of SLSNe I, in that they are $\sim$7000 km s^{-1} slower.

5 LATE TIME SPECTRA AND SIGNS OF INTERACTION IN SLSNE II

In Fig. 10, we show the late VLT+FORS2 spectrum of SN2103hx and those of PS15br obtained with VLT+Xshooter and NTT+EFOSC2, which are the latest spectra and the only late (>150d from peak) phase for SLSNe II obtained to date. For SN2103hx, a lower S/N spectrum was taken by PESSTO on +210 d, and this is also shown in Fig. 10. This NTT spectrum does not appear to be significantly different to the FORS2 +237-d spectrum and as it is much lower quality, we will not discuss it further. In the case of PS15br, PESSTO spectra do not show any substantial evolution with respect to those of XShooter and have lower S/N; hence, we focus our analysis only on the XShooter spectra.

There is no distinguishable line at the position of [O I] $\lambda\lambda$6300, 6364 Å, which is usually prominent in core-collapse SNe. There is perhaps some hint of weak and broad emission in SN2103hx that could be attributed to this line, but the detection is $\lesssim 2\sigma$ with respect to the continuum flux and is not convincing (see Fig. 11). In Fig. 11, we compare our SN2103hx spectrum with those of the fast-declining SN II (or SN IIL) SN1980K and the broad-line SN Ic SN1998bw at late epochs and scaled to the same luminosity distance of SN2103hx (570.3 Mpc) in order to match the rest-frame spectral luminosity exhibited by SN2013hx. The spectra of SN2013hx and SN1980K are similar, although they differ by 135 d with respect to the peak epochs, and as a consequence are also similar to that of PS15br shown in the bottom plot. The overall similarity with SNe IIL suggests that SLSNe II are also consistent with a star explosion similar in mass to those of normal core-collapse SNe. The H α profile and the blueward features are also different from that of iPTF13ehe, a SLSN I with late-time interaction with a hydrogen shell. The width of the central and blue components of SN2013hx H α are comparable with those of PS15br at $\sim$337 d. The PS15br H$_\beta$ emission component is stronger than those of SN2013hx and SN1980K that are almost non-existent.

The +247 d SN2103hx spectrum and all the late PS15br spectra are dominated by a strong and multicomponent H α profile, and the simplest explanation would be that the SN ejecta are interacting with an H-rich, highly asymmetric CSM (as previously suggested for similar late-time interactions; e.g. Benetti et al. 2016). There are no other lines visible in the optical with the exception of H β, and the continuum is faint. However, as shown in Fig. 10 (bottom panel), the PS15br NIR spectra exhibit Paschen lines in emission, as well as He I λ10830, which obscures Paγ. We note that both H β and Paα profiles resemble that of H α with a prominent blue shoulder. In SN2103hx, the H β flux is $\sim$50 times less than that of the H α profile and $\sim$30 times less than the H α central component (see Table 4). For case B recombination in the temperature regime $2500 \leq T(\mathrm{K}) \leq 10\,000$ and electron density $10^2 \leq n_e \leq 10^6$ the H α line should be three times stronger than H β. However, the case B recombination is never observed in SNe II before a couple of years as both the $n = 4 \rightarrow n = 2$ (H β) and $n = 3 \rightarrow n = 2$ (H α) transitions are optically thick (Xu et al. 1992). In this case, the Pα ($n = 4 \rightarrow n = 3$) transition will depopulate the $n = 4$ state, with the photons escaping to produce the Pα emission line. However, H α is produced strongly, because the only other alternative for depopulation of the $n = 3$ state is Lyman β. In PS15br, the H β flux is $\sim$10 times less than that of the H α profile and, as expected, the Pα emission line is visible. The integrated luminosity of the overall profile of the H α line is $\sim$9 and $\sim$20 times those of a normal SN II at a similar phase (Kozma & Fransson 1998) for SN2103hx and PS15br, respectively. This suggests an additional contribution to H α luminosity in both cases. What powers the decline rate of the late-time light curve is an open question. One could speculate that the signature of interaction we see at this late phase is indicative of the same powering source for the light curves between 100 and 260 d. Late interaction has been observed in bright SNe IIL such as SNe 1979C, 1980K and 1986E (see Fesen et al. 1999; Cappellaro, Danziger & Turatto 1995; Benetti et al. 2016, and references therein).

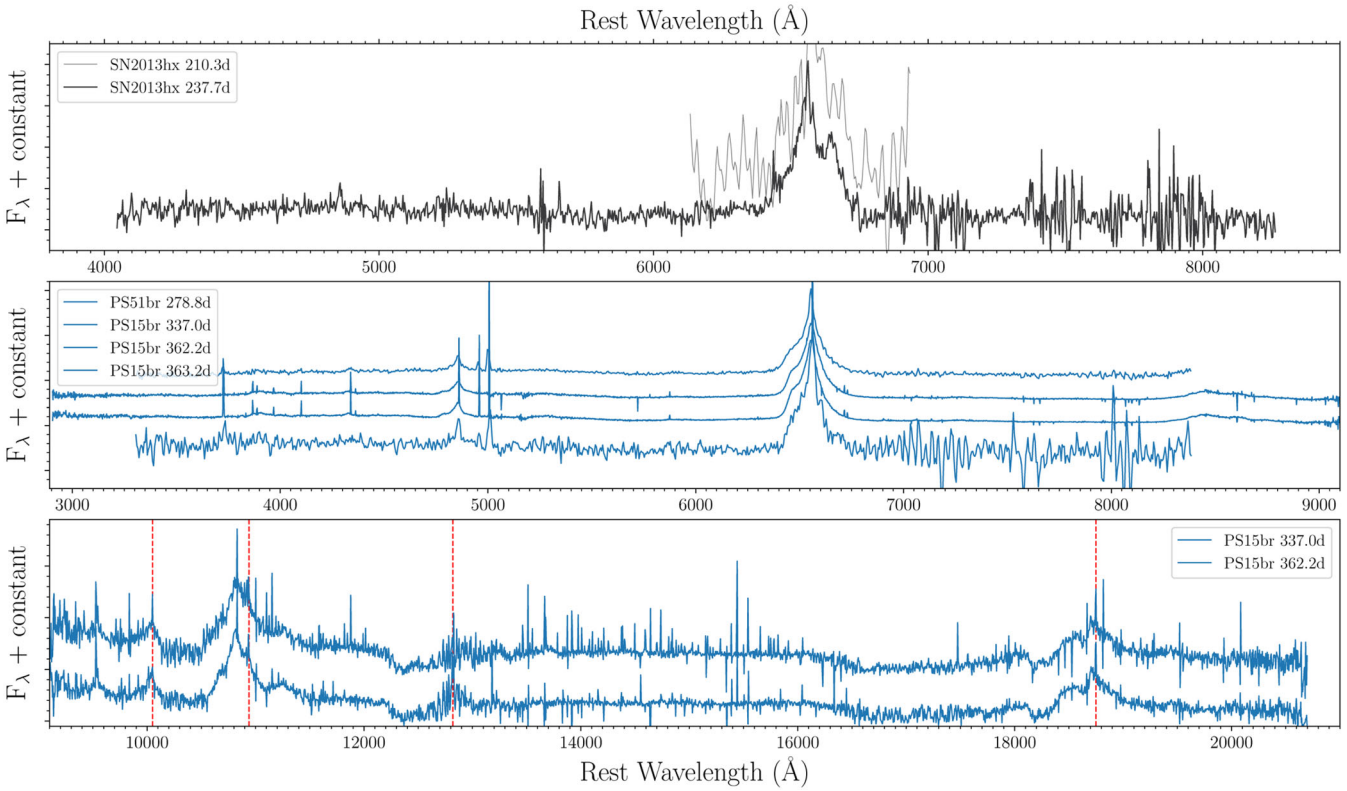

Figure 10. Top: last two spectra of SN2103hx. Middle: late-time optical spectra of PS15br. Bottom: late-time NIR spectra of PS15br. Paschen lines from α to δ are identified by vertical dashed red lines.

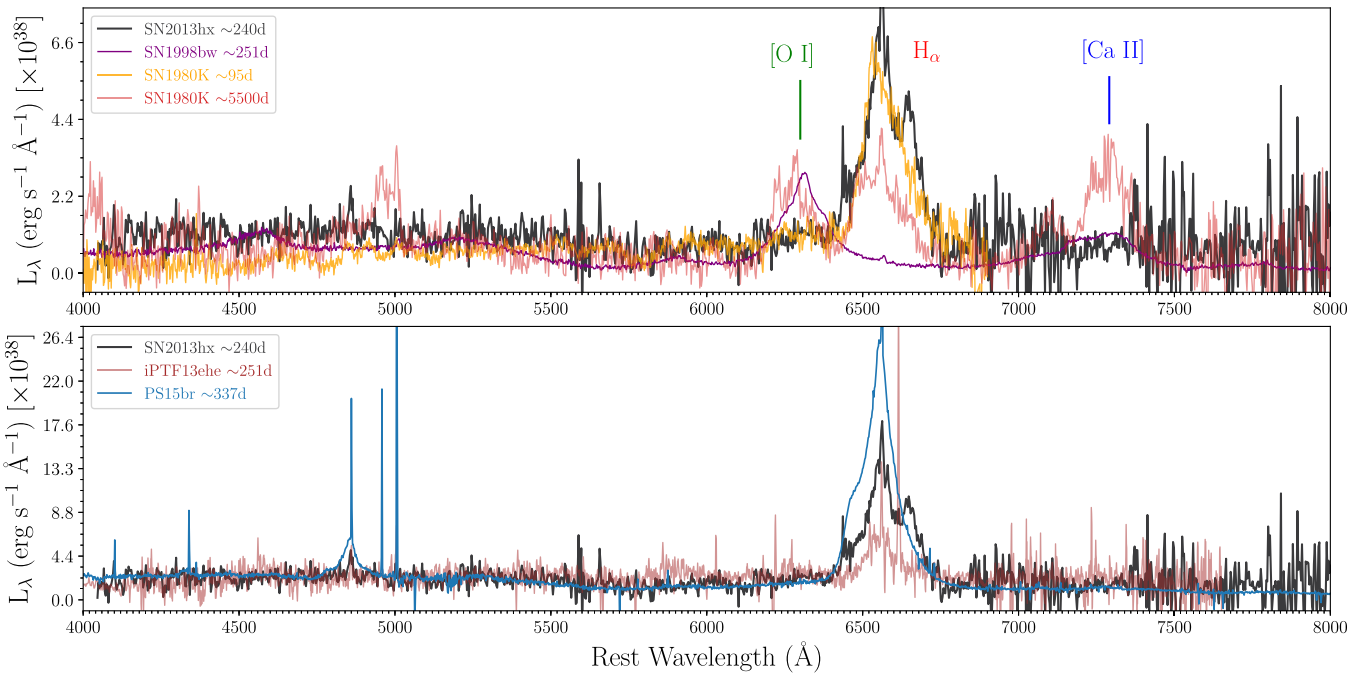

Figure 11. Top: the VLT+FORS2 spectrum of SN2103hx compared with late spectra of the SNe IIL SN1980K (Barbon et al. 1982) and a late spectrum of the broad-line SN Ic SN1998bw (Patat et al. 2001). All the spectra have been scaled to the continuum flux level of SN2103hx. The most prominent lines of nebular core-collapse spectra are labelled. Bottom: the VLT+FORS2 spectrum of SN2103hx and the VLT+XShooter (337d) compared with SLSNe I iPTF13ehe, a slow SLSN I showing late H α emission.

Table 4. Late Hα profile measurements of SLSNe II SN2103hx (∼240 d) and PS15br (∼337 d).

Feature	Peak (Å)	Width (Å)	Width (km s^{-1})	Velocity wrt Hα peak (km s^{-1})	Flux (erg s^{-1} cm^{-2})
			SN2103hx		
Blue	6459.8	73.8	3427	−4700	1.1×10^{-16}
Central	6558.9	73.8	3376	−190	4.0×10^{-16}
Red	6650.8	73.8	3329	4000	2.2×10^{-16}
			PS15br		
Blue	6460.7	66.8	3102	−4700	2.4×10^{-16}
Central	6556.5	105.2	4813	−320	9.3×10^{-16}

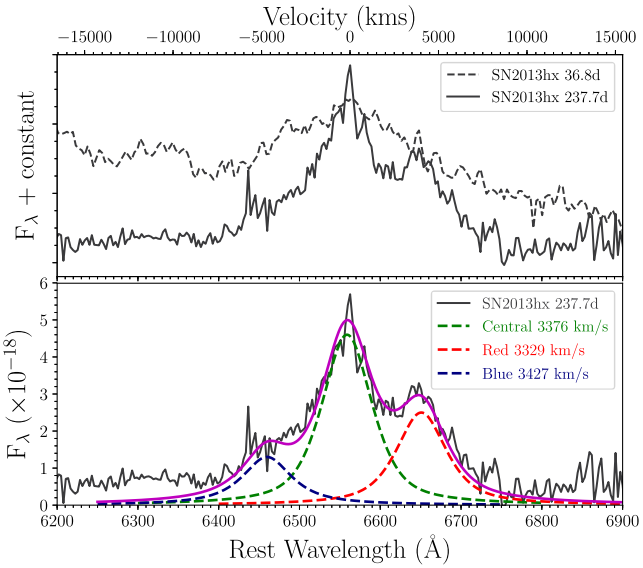

Figure 12. Top: Hα multicomponent profile of the SN2103hx spectrum at 238 d (black solid line) with that exhibited at 37 d (black dashed line) scaled in flux to match the previous spectrum. Bottom: Hα multicomponent profile of the spectrum at 238 d since maximum. The spectrum is dominated by interaction with a H-rich CSM.

The SN2103hx Hα profile in Fig. 12 has a triple peak structure spanning 7400 km s^{-1} across the base (see Table 4), which is similar to the triple peak shown by the interacting SN II PTF11iqb after 500 d (Smith et al. 2015). The central component is consistent with having zero rest-frame velocity, and the blue component peaks at −4700 km s^{-1} with respect to this Hα rest-frame velocity. This blue component appears to be the weakest of the three. The red component is at +4000 km s^{-1}. We analysed the feature with Gaussian, Lorentzian and pseudo Voigt line profiles, having set a priori the number of components (three) but letting the width and intensity of each component vary. We retrieved the best fit with three Voigt profiles with widths of ∼3400 km s^{-1}. However, Gaussians have a similar goodness of fit and produce similar linewidths but different line fluxes. We performed the same analysis on the 337-d spectrum of PS15br. In this case, Hα shows a two-component profile, a blue at −4700 km s^{-1} with respect to (wrt) Hα and a central at almost zero rest-frame velocity (−390 km s^{-1}). This profile is similar to that shown by SN2103hx, with the exclusion of the red component, and it is also shown in the Paα (see middle panel of Fig. 13) but not in Paγ, which is blended with the more prominent He I λ10830. The best fit for these components is retrieved with Voigt profiles of width ∼3100 and ∼4800 km s^{-1} for the blue and central components, respectively (see Fig. 13).

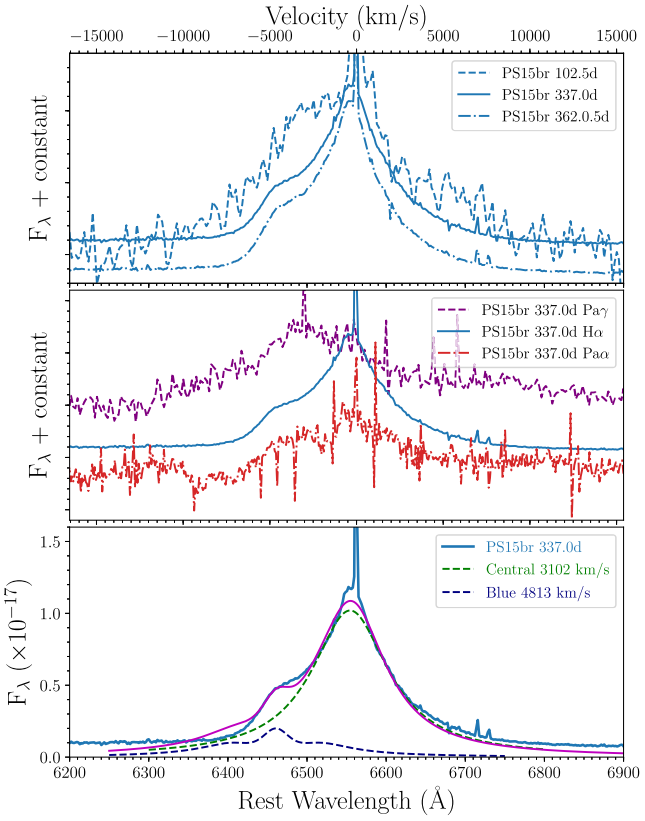

Figure 13. Top: Hα multicomponent profile of the PS15br spectrum at 337 and 362 d (blue lines) with that exhibited at 102 d (cyan line) scaled in flux to match the previous spectrum. Middle: Hα (blue line), Paγ (magenta line) and Paα (red line) multicomponent profiles of the PS15br spectrum at 337 d. Bottom: Hα multicomponent profile of the PS15br spectrum at 337 d since maximum. The spectrum is dominated by interaction with a H-rich CSM.

In general, the line profile could be schematically explained by the following:

(i) a relatively broad emission from the SN ejecta with FWHM ∼3400 km s^{-1};
(ii) interaction of the H-rich ejecta with

(a) a ring/disc edge-on;
(b) a dense, clumpy CSM;

(iii) a likely unshocked CSM that could explain the narrow, unresolved emission on the top of the central component.

The blue wing of the Hα emission of SN2103hx and PS15br roughly coincides in wavelength with the corresponding blue wing of the Hα profile at 37 and 102 d, as shown by the top panels of

Figs 12 and 13. If the absorption minimum maintains the same velocity shown at early time, it will be at a similar wavelength to the peak of the blue component. However, if SLSNe II evolution follows closely that of fast-declining SNe II, as suggested by the spectroscopic evolution (see Section 3.2 and Fig. 11), we would not expect any absorption component from the Hα able to dim the blue peak. Instead, an asymmetric, clumpy CSM could explain the difference in intensity between the blue and red components in SN2103hx and the absence of a red component in PS15br. If we considered the blue component of SN2103hx to be a consequence of a boxy profile, and hence more a shoulder than a peak, we would still need to invoke an asymmetric configuration. Such CSM structure would have a two-component wind with a spherically symmetric region responsible for the boxy profile and the presence of a denser clump in the direction opposite to that of the observer in order to explain the intensity of the red component in SN2103hx. Hence, both scenarios would suggest an asymmetric configuration of the CSM. Such configurations have been invoked to explain late-time multicomponent Hα profiles for several SNe II (e.g. Uomoto & Kirshner 1986; Fesen et al. 1999; Pozzo et al. 2004; Inserra et al. 2011; Benetti et al. 2016).

6 DISCUSSION

SN2103hx and PS15br provide, for the first time, a small sample of SLSNe II useful for the understanding of the hydrogen-rich SLSNe. These SLSNe are different from those undergoing strong interaction with an optically thick CSM, showing spectra with strong optical lines having multiple emission components, such as SN2006gy (Smith et al. 2007). They have luminosity spanning from $-20 > M_g > -22$, similar spectral evolution and an origin in faint host galaxies. The latter is surprisingly similar to the characteristic locations of their hydrogen-free counterparts (Lunnan et al. 2014; Chen et al. 2015; Leloudas et al. 2015a). Their photospheric (<100 d) spectroscopic evolution resembles those of bright SNe II (or SNe IIL) with a delay of 15–20 d and their light curves show a linear decline over 100 d post-peak. Hence, they are more luminous and evolve more slowly than normal SNe IIL. These two characteristics (more luminous, slower evolution) also link SLSNe I to normal SNe Ic in a similar way. Therefore, it might be that the power source responsible for the differences between SLSNe I and SNe Ic is also accountable for those between SLSNe II and SNe II.

The extreme luminosity of SLSNe I has been explained with a few scenarios and we use our data set to constrain similar models for the origin of SLSNe II. The light curves that we use in the following sections are the full, estimated, bolometric light curves that have been corrected for flux missed in both UV and NIR, as described in Section 4.2.

6.1 ^{56}Ni driven explosion

To test if radioactive heating could be the main source of energy, we can assume that γ-rays from ^{56}Co decay are fully thermalized and can hence estimate the ^{56}Ni mass needed for these events, comparing their bolometric luminosity with that of SN1987A. For SN2013hx, the peak would require a ^{56}Ni mass of $M(^{56}\mathrm{Ni}) \sim 8.0\ \mathrm{M}_\odot$ and the luminosity in the tail phase at around 140 d would be $M(^{56}\mathrm{Ni}) \sim 1.0\ \mathrm{M}_\odot$. For PS15br, the luminosity at 100 d would require $M(^{56}\mathrm{Ni}) \sim 2.2\ \mathrm{M}_\odot$. Although these objects are H-rich and hence hydrogen recombination should play some role in the photospheric phase of the light curve, we applied our toy model (see Appendix D of Inserra et al. 2013b) to have an alternative estimate of the ^{56}Ni mass required to power the late light curves. We retrieved values of $4.3 < M(^{56}\mathrm{Ni}) < 8.4\ \mathrm{M}_\odot$ for SN2013hx (depending on whether or not we included the tail phase data after 142 d) and $M(^{56}\mathrm{Ni}) \sim 4.4\ \mathrm{M}_\odot$ for PS15br, for which we do exclude the tail as our first late spectrum showing interaction is coincident with the first photometric point of the tail.

Although there is some uncertainty in these numbers, the large ^{56}Ni masses could suggest a pair instability explosion (Barkat, Rakavy & Sack 1967; Fraley 1968). However, because of the large ejecta masses expelled in pair instability explosions, the rise times of the light curves are a factor of 2–3 greater than that observed in our objects (Woosley, Blinnikov & Heger 2007). In the case of pair instability, the ejecta masses should be two to five times greater than the ^{56}Ni mass (Umeda & Nomoto 2008) and such an amount of material would be mainly composed of He ($>13\ \mathrm{M}_\odot$) and H ($>11\ \mathrm{M}_\odot$) leading to a long plateau in their light curves (Woosley & Weaver 1995). This has not been observed, implying that the late-time evolution of the light curves of SN2103hx and PS15br is not driven by ^{56}Ni but is due to some late interaction (see Section 5).

6.2 Circumstellar medium interaction

In SN2103hx, PS15br and SN2008es, we do not observe narrow and intermediate features, which suggests an ongoing interaction with a CSM. However, we cannot exclude, a priori, such a scenario because if the CSM is opaque and the shock encounters no further CSM at larger radii, the usual signatures of interaction spectra can be avoided (Smith & McCray 2007; Chevalier & Irwin 2011). This could, in principle, explain the spectra evolution in the the objects.

The dense CSM can be produced by a wind or by a shell ejected prior to the SN explosion. In the former case, following the model of Blinnikov & Bartunov (1993) used to explain SNe IIL, a dense stellar wind that reprocesses the UV photons produced at shock breakout can boost the luminosity up to superluminous magnitudes. This would need an increase in the mass-loss rate by one to two orders of magnitude, with respect to those observed in red supergiants (RSGs), and hence reaching $\dot{M} \sim 10^{-3}\ \mathrm{M}_\odot\ \mathrm{yr}^{-1}$. However, in this scenario after ~50–80 d from peak, the light curve should show a drop in magnitude. The higher the peak luminosity, the greater the drop, with at least a decrease of 2 mag in a superluminous case – and a subsequent settling on to a ^{56}Co tail. Our data set, including SN2008es, does not show such a drop around that phase or even later.

From the blackbody fit to the SED (see Section 4.4) and the bolometric luminosity (see Section 4.2), we can estimate the peak radius of SN2103hx and PS15br to be 3×10^{15} cm and 2.3×10^{15} cm, respectively. These radii are a factor of 30 and 10 greater than that of a large RSG (Smith et al. 2001) and, as a consequence, the opaque CSM shell forming the envelope is not bound to the star. Following the formalism of Quimby et al. (2007); Smith & McCray (2007), the peak luminosity produced by the radiation emitted by a shocked, thermalized shell is

$$L \propto \frac{M_{\mathrm{sh}} v_{\mathrm{ph}}^2}{2\, t_{\mathrm{max}}}, \quad (1)$$

where M_{sh} is the mass of the dense CSM shell, v_{ph} is the velocity of the pseudo-photosphere and t_{max} is the rise time. Assuming a rise time of 37 d for SN2103hx and 35 d for PS15br (see Section 3.1) and a pseudo-photosphere of 6000 km s^{-1} (see Section 4.4), we can infer 2.5 and 0.5 $\mathrm{M}_\odot$ for the CSM masses of SN2103hx and PS15br, respectively.

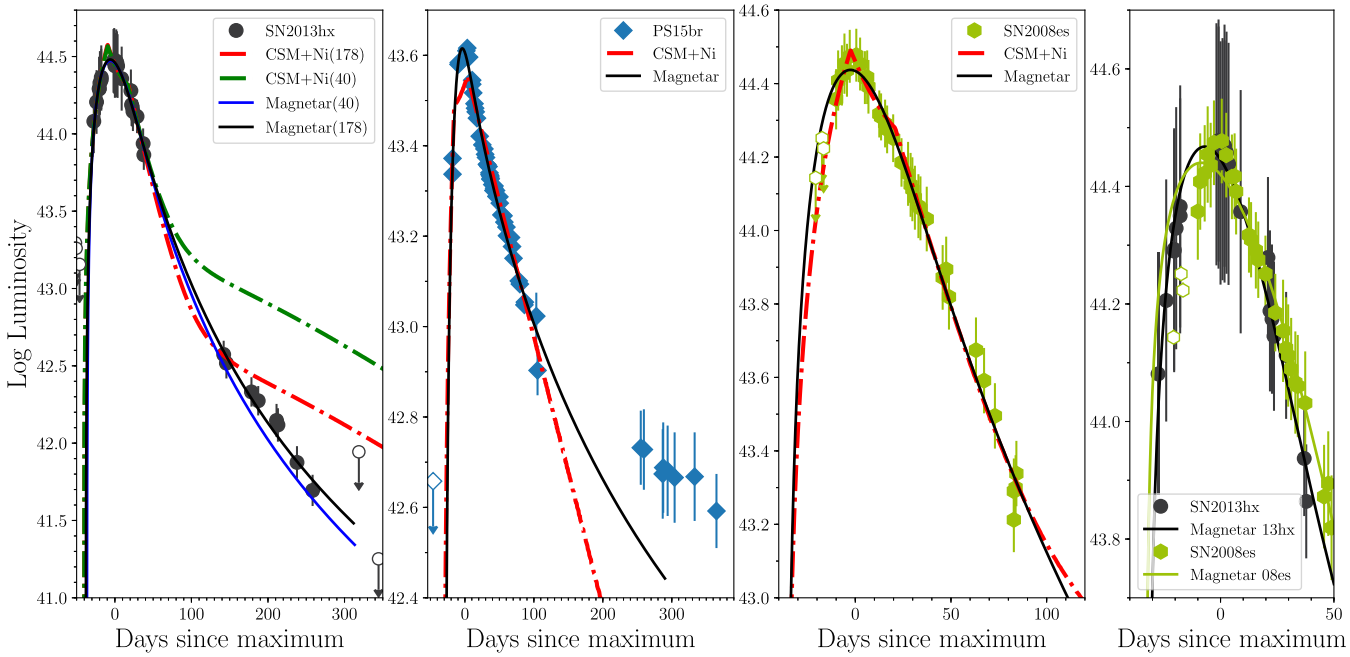

Figure 14. Bolometric light curves of SN2103hx, PS15br and SN2008es compared with the best-fitting models. The black solid line (and also the blue for SN2103hx) refers to the magnetar model, while the red dot-dashed (and also the green for SN2103hx) refers to the CSM+Ni model. Limits are shown as empty symbols. For the case of SN2103hx, the (40) models consider up to 40 d past maximum, while (178) refers to the models considering up to 178 d. The plot on the far right shows a comparison of bolometric light curves and magnetar fit around maximum light for SN2013hx and SN2008es. This highlights how the different time baseline coverage gives slightly different magnetar parameters (see Table 6).

Table 5. Best-fitting parameters for the CSM+Ni model, which has nine free parameters.

Object	t_{rise} (d)	M_{CSM} ($M_\odot$)	M (^{56}Ni) ($M_\odot$)	M_{ej} ($M_\odot$)	χ^2/dof
SN2103hx[a]	40.35/40.35	2.35/2.37	2.02/0.61	9.81/10.48	0.8/20 1.12/28
PS15br	31.90	2.09	0.00	12.94	500.5/55
SN2008es	36.41	2.75	1.14	9.46	5.4/30

Note. [a]The first values refer to the model considering only the first 40 d, while the second values refer to the model considering up to 178 d.

The aforementioned radii imply a wind distance of 300 and 150 au for the two objects. Inferring a wind velocity of 10–100 km s^{-1} (which brackets RSG and faster luminous blue variable wind velocities), the wind must have begun ∼10–100 yr before the explosion of SN2103hx and ∼7–70 yr before that of PS15br. Hence, the mass-loss rates would be 0.03–0.25 and 0.007–0.07 $M_\odot$ yr^{-1}, which are too large to be produced by a normal steady stellar wind (Smith 2014). Therefore, if a dense CSM scenario is invoked as the explanation of the peak luminosity, it would suggest an unbound CSM shell configuration.

In order to reproduce the bolometric light curves of SN2103hx, PS15br and SN2008es, we use a semi-analytical code based on the equations of Chatzopoulos, Wheeler & Vinko (2012) and implemented by Nicholl et al. (2014). We use the model considering both the CSM shell and radioactive decay of the ^{56}Ni contribution to the light curves, setting $\delta = 2$ and $n = 12$ for the SN ejecta inner and outer power-law density profile slopes, respectively, in all cases. We assume Thomson scattering to be the dominant source of opacity with a solar mixture of mass fraction ($X = 0.7$), which gives an opacity $\kappa = 0.2(1 + X) = 0.34\,\mathrm{cm^2\,g^{-1}}$, which is the standard value for a hydrogen- and helium-rich ejecta. An identical configuration was previously used by Chatzopoulos et al. (2013) to fit the bolometric light curve of SN2008es. Our best fits are shown in Fig. 14 (red dot-dashed line), while their parameters are reported in Table 5. We did not fit the tail of PS15br because that is the result of interaction. As the late SN2103hx tail might be dominated by interaction – with a different and probably less dense component (see Section 5) – we made two illustrative fits. First, we fitted the light curve using data up to 40 d after maximum, and then a second using all data out to 178 d (before the clear inflection in slope; see Sections 3.1 and 4.2) and before the first spectrum showing interaction with another CSM (at 210 d; see Section 3.2). We derive $2.1 \lesssim M_{CSM} \lesssim 2.7\,M_\odot$, $0.0 \lesssim M(^{56}\mathrm{Ni}) \lesssim 2.0\,M_\odot$ and $9.5 \lesssim M_{ej} \lesssim 12.9\,M_\odot$. Following the same methodology, we also estimate that a wind of 2.6 and 2.3 $M_\odot$ (or 4.7 and 3.9 $M_\odot$ in the case of dense shell configuration) is responsible for the late interaction of SN2103hx and PS15br, respectively. The ^{56}Ni masses are consistent with the aforementioned limit and the CSM mass is consistent with observation of a pseudo-photosphere at the velocity reported in Section 4.4. This mass is of the order of that associated with impulsive mass ejections, as discussed in Smith & Owocki (2006). However, the ejecta masses are at least a factor of 2 greater than is expected to avoid an optical plateau from hydrogen recombination, while the total masses (ejecta+CSM+remnant) lie at the upper end of those observed and theorized for SNe II (Smartt 2009; Janka 2012; Smartt 2015). Such CSM masses are more similar to those of stripped-envelope SNe

Table 6. Best-fitting parameters for magnetar modelling, which has four free parameters, of the bolometric light curves and χ^2/dof value, together with the derived parameters (last two columns).

Object	τ_m (d)	B_{14}	P_{ms}	t_0 (MJD)	χ^2/dof	E^{mag} (10^{51} erg)	M_{ej} ($M_\odot$)
SN2103hx[a]	36.71/38.15	1.31/0.89	2.22/2.29	56643.20/56641.57	0.6/15 1.61/23	3.38/5.24	6.95/5.20
PS15br	17.60	1.61	6.38	57056.27	161.5/50	0.39	1.93
SN2008es	36.58	0.97	2.35	54578.28	5.0/25	2.66	5.71

Note. [a]The first values refer to the model considering only the first 40 d, while the second values refer to the model considering up to 178 d.

and not of SNe II. This two-component wind CSM configuration that is required to explain the late interaction of SN2103hx and PS15br, is difficult to explain with a single steady wind.

6.3 Internal energy source

Despite the potential of the CSM scenario to describe the main observational data – light curves and spectra evolution – and the overall picture observed in SLSNe II, there are still some details that would be easier to explain with a central engine that deposits its energy into a supernova explosion and significantly enhances the luminosity.

As observed in Section 4.2, PS15br has an asymmetric light curve that might be difficult to explain with a CSM interaction, as also shown in Fig. 14. In addition, SLSNe II have bell-shaped light curves around peak only a factor of 1.2 wider than those of SLSNe I. Furthermore, they show similar spectra and temperature evolution to those of fast-declining SNe II but delayed by 15–20 d in a similar fashion to what is shown between SLSNe I and stripped envelope SNe. In addition, they share similar faint host galaxies as those of SLSNe I.

For these reasons, we fit our light curves with our semi-analytical diffusion model presented in Inserra et al. (2013b) in which a rapidly spinning magnetar deposits its rotational energy into a supernova explosion, through magnetic dipole radiation, and significantly enhances the luminosity.[6] Then, we treat for γ-ray leakage from ejecta as in Chen et al. (2015), which is similar to the prescription of Wang et al. (2015). The magnetar luminosity depends primarily on two parameters, the magnetic field strength B_{14} (expressed in terms of 10^{14} G) and the initial spin period P_{ms} (in ms). As previously done with the interaction model, we used an opacity $\kappa = 0.34\,cm^2\,g^{-1}$. Table 6 lists the best-fitting parameters for each object, and Fig. 14 shows the fits (black solid line). As the reduced χ^2 ($\chi^2_{red} = \chi^2$/dof) fitting gives good matches to models without ^{56}Ni, we have no need to introduce ^{56}Ni as an additional free parameter. As in the case of CSM model fitting for SN2103hx, we perform two fits (only using data up to 40 d and then using all data up to 178 d), which in this case are very similar. However, for PS15br we only fit the early light curve up to ∼102 d. The light curves of our two objects are well reproduced but the late luminosity of the model for SN2103hx is better reproduced by the 40-d magnetar model. These data points may already have an additional luminosity contribution due to some late interaction (as seen in the late spectra), and hence a light curve dimmer than these points would favour such a model. This is also true for PS15br where the magnetar model is dimmer than the late time points where the luminosity is driven by interaction. The CSM models are too bright to describe SN2103hx data after ∼180 d. Furthermore, if we remove the ^{56}Ni contribution, we obtain a worse χ^2_{red} and a luminosity at late time still brighter than the data. The magnetar fit for PS15br is better than that of the CSM as testified by the χ^2_{red} values of Tables 5 and 6, despite the latter having a higher number of free parameters. The magnetar fit to SN2008es is not as satisfactory as the CSM fit, as the data show a faster rise than the best-fitting model. However, the results of SN2008es fit are in agreement with that of Kasen & Bildsten (2010).[7] One can ask why SN2103hx and SN2008es end up with different results if their light-curve behaviour is so similar. As shown in the right panel of Fig. 14, the reason is that we have different time coverage for each. The light-curve data for SN2008es stretch to 80 d after peak whereas the data for SN2103hx stop at 50 d, and there are more pre-peak detection points for SN2013hx than for SN2008es (which has only limits before −10 d).

We further estimated velocity and temperature evolution from the light-curve fits to ejecta mass and kinetic energy. In Fig. 15 we show that the temperature evolution of the magnetar model matches the observed ones reasonably well and better than the interaction model, which produces results that are always too hot. Photospheric velocities are slightly faster than the Fe II velocities, which trace the photospheric evolution. The sudden drop to zero of both temperature and velocity evolution of the best-fitting model for PS15br occurs because more than half of the core has been exposed. This is a consequence of the low energy and ejecta mass needed to fit the light curve.

Another possible central engine is that of the fall-back accretion (Dexter & Kasen 2013), which can give a similar asymptotic behaviour of the light curve ($L_t \propto t^{-5/3}$) with respect to the magnetar engine but would have lower luminosity than that observed after 180 d in SN2103hx. However, this scenario implies photospheric velocities higher than that shown by our sample and would fail to reproduce the PS15br light curve as models considering H recombination have longer rise times and a bump 200 or 300 d after the explosion. To better investigate this scenario, a dedicated fit for these objects is required.

7 CONCLUSION

We have presented extensive photometric and spectroscopic coverage of two superluminous, hydrogen-rich supernovae with light curves covering from weeks before peak up to 260 d (SN2103hx) and 365 d (PS15br). We then analysed the two objects together with the only other SLSN II (SN2008es) to search for similar observational behaviours, suggesting that they exist as superluminous events rather than superluminous interacting events (i.e. SLSNe IIn) or SLSNe I.

[6] The semi-analytical code is available at: https://star.pst.qub.ac.uk/wiki/doku.php/users/ajerkstrand/start.

[7] This is expected, as in Inserra et al. (2013b) we already tested our code with respect to that of Kasen & Bildsten (2010).

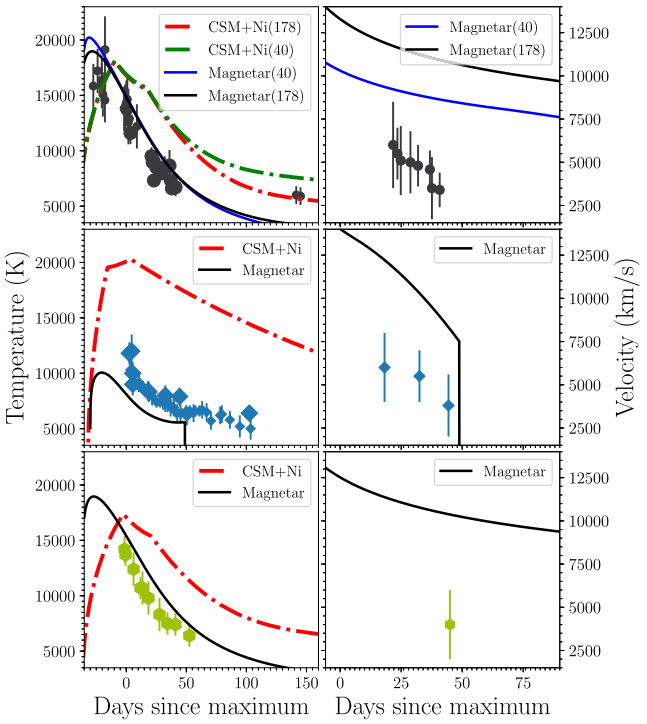

Figure 15. Temperature and velocity evolution (only for the Fe II lines tracing the photospheric evolution) of SN2103hx, PS15br and SN2008es compared with the best-fitting models. The black solid line (and also the blue for SN2103hx) refers to the magnetar model, while the red dot-dashed (and also the green for SN2103hx) refers to the CSM+Ni model. Symbols are the same as Fig. 15.

SN2103hx has $M_g = -21.7$ mag and $L_{\rm bolometric} \approx 2.75 \times 10^{44}$ erg s^{-1} at peak, while PS15br shows $M_g \sim -20.2$ and $M_U \leq -20.8$ mag and $L_{\rm bolometric} \approx 4.15 \times 10^{43}$ erg s^{-1} at maximum light. The former has a post-peak light-curve decline similar to that of SN2008es and normal SNe IIL, whereas PS15br shows an initial decline comparable to that of SN2103hx and SN2008es and a second, slower decline similar to those shown by transitional SNe IIn/II events at normal luminosity. Although PS15br luminosity is fainter than SN2103hx and SN2008es, we have considered it a bona fide SLSN II due to its spectroscopic evolution similar to that of SN2103hx and PS15br and a spectrophotometric evolution dissimilar to any other H-rich SN in a similar luminosity space.

For PS15br, we also obtained an epoch of broad-band polarimetry at 6 d after maximum. After correcting for the ISP and the polarization bias, we retrieved a polarized value of $P = 0.94 \pm 0.17$ per cent. However, this value strongly depends on the assumed ISP and hence no conclusive evidence on the source of the polarization associated with PS15br can be derived.

SLSNe II (such as SN2008es, SN2103hx and PS15br) show a spectroscopic evolution dominated by Balmer, He, Ca, Fe and other metal lines and an emission feature at early times at ∼4600 Å, identified as C III/N III. SN2103hx and PS15br show a late interaction (phase > 140 d and >250 d, respectively) due to an asymmetric, clumpy CSM that dominates the late light-curve behaviour. Regardless of the peak luminosity, SLSNe II spectroscopic and temperature evolution resembles those of fast-declining SNe II (or SNe IIL) with a delay of 15–20 d. This suggests that the transients are linked to SNe II in a similar fashion as SLSNe I are linked to SNe Ic.

We applied two semi-analytical codes to fit the light curves of all SLSNe II. The first is based on the interaction between the ejecta and a dense uniform shell of H-rich material, while the second is based on a diffusion model with energy input from a spinning-down magnetar. We were able to reproduce the available bolometric light curve with $2.1 \lesssim M_{\rm CSM} \lesssim 2.8$ M$_\odot$ and $9.5 \lesssim M_{\rm ej} \lesssim 13.0$ M$_\odot$, while the late-time light curve exhibited by SN2103hx and PS15br and driven by interaction can be fitted with a wind of 2.6 and 2.3 M$_\odot$ or a dense shell of 4.7 and 3.9 M$_\odot$, respectively. All light curves are also reproduced with feasible physical values for a magnetar including the data at 140–180 d of SN2103hx, when the luminosity of our best-fitting model is lower than the data, which are already due to the aforementioned late interaction. To fit these, we require $0.9 \lesssim B_{14} \lesssim 1.6$ and $2.2 \lesssim P_{\rm ms} \lesssim 6.4$ consistent with B of known galactic magnetars ($B_{14} \sim$ 1–10) and with physically plausible periods ($P_{\rm ms} > 1$). We derived energies of $0.4 \lesssim E^{\rm mag} \lesssim 5.2$ 10^{51} erg and ejected masses of $1.9 \lesssim M_{\rm ej} \lesssim 6.9$ M$_\odot$. Both scenarios have their weaknesses. The high ejecta masses retrieved by the interaction model and the spectroscopic similarities to bright, linear SNe II regardless of the peak luminosity, would tend to disfavour the interaction scenario. However, these characteristics can be better explained by the magnetar scenario. However, at least for the case of PS15br, some weak interaction is present for the majority of the photospheric evolution in a similar fashion to that found for some SLSN I (Inserra et al. 2017c). In addition, the interaction shown at a late phase by SN2103hx and PS15br does not allow a firm conclusion and suggests that interaction could play a role in the evolution of SLSNe II.

Despite our data set and analysis of this first sample of SLSNe II, open questions remain, as follows.

(i) Do SLSNe II with interaction-free light curves exist? What should their luminosity be and what are the line profiles expected in a truly nebular spectrum?

(ii) What is the role of metallicity in the progenitor star evolution that will produce an H-rich SLSNe? It appears that they are all associated with faint dwarf galaxies and possibly low-metallicity progenitors such as those of SLSNe I.

(iii) Can the geometry of the explosion play a role in the observables and/or shed light on the powering mechanism or their light curves?

As for the case of SLSNe I, to address these topics, high-quality data and their modelling at early phase or in an interaction-free nebular phase are needed to determine the ejecta masses, composition and the mass of ^{56}Co contributing to the luminosity. This seems the most likely way to make progress.

ACKNOWLEDGEMENTS

SJS acknowledges funding from the European Research Council under the European Union's Seventh Framework Programme (FP7/2007-2013)/ERC Grant agreement no. [291222] and STFC grants ST/I001123/1 and ST/L000709/1. MF is supported by a Royal Society–Science Foundation Ireland University Research Fellowship. EEEG acknowledges support for this work by the Deutsche Forschungsgemeinschaft through the TransRegio project TRR33 'The Dark Universe'. SB is partially supported by the PRIN-INAF 2014 project Transient Universe: unveiling new types of stellar explosions with PESSTO. Support for IA was provided by National Aeronautics and Space Administrati (NASA) through the Einstein Fellowship Programme, grant PF6-170148. KM acknowledges support from the STFC through an Ernest Rutherford Fellowship. SP and RC acknowledge support from EU/FP7-ERC grant no. [615929]. SS acknowledges support from CONICYT-Chile

FONDECYT 3140534, Basal-CATA PFB-06/2007 and Project IC120009 'Millennium Institute of Astrophysics (MAS)' of Iniciativa Científica Milenio del Ministerio de Economía, Fomento y Turismo. This work was partly supported by the European Union FP7 programme through ERC grant number 320360. Part of this research was conducted by the Australian Research Council Centre of Excellence for All-sky Astrophysics (CAASTRO), through project number CE110001020. Pan-STARRS is supported by the University of Hawaii and NASA's Planetary Defense Office under Grant No. NNX14AM74G. The Pan-STARRS1 Sky Surveys have been made possible through contributions by the Institute for Astronomy, the University of Hawaii, the Pan-STARRS Project Office, the Max Planck Society and its participating institutes, the Max Planck Institute for Astronomy, Heidelberg and the Max Planck Institute for Extraterrestrial Physics, Garching, Johns Hopkins University, Durham University, the University of Edinburgh, the Queen's University Belfast, the Harvard-Smithsonian Center for Astrophysics, the Las Cumbres Observatory Global Telescope Network Incorporated, the National Central University of Taiwan, the Space Telescope Science Institute, and the National Aeronautics and Space Administration under Grant No. NNX08AR22G issued through the Planetary Science Division of the NASA Science Mission Directorate, the National Science Foundation Grant No. AST-1238877, the University of Maryland, Eotvos Lorand University (ELTE), and the Los Alamos National Laboratory. This work is based (in part) on observations collected at the European Organization for Astronomical Research in the Southern hemisphere, Chile as part of PESSTO, (the Public ESO Spectroscopic Survey for Transient Objects Survey) ESO programmes 188.D-3003 and 191.D-0935. Some of the data presented herein were obtained at the Palomar Observatory, California Institute of Technology. The Liverpool Telescope is operated on the island of La Palma by Liverpool John Moores University in the Spanish Observatorio del Roque de los Muchachos of the Instituto de Astrofisica de Canarias with financial support from the UK Science and Technology Facilities Council.

REFERENCES

Agnoletto I. et al., 2009, ApJ, 691, 1348
Alam S. et al., 2015, ApJS, 219, 12
Alard C., 2000, A&AS, 144, 363
Ambikasaran S., Foreman-Mackey D., Greengard L., Hogg D. W., O'Neil M., 2014, IEEE Transactions on Pattern Analysis and Machine Intelligence, 38, 2 (arXiv:1403.6015)
Anderson J. P. et al., 2014a, MNRAS, 441, 671
Anderson J. P. et al., 2014b, ApJ, 786, 67
Arcavi I. et al., 2016, ApJ, 819, 35
Baltay C. et al., 2007, PASP, 119, 1278
Barbon R., Ciatti F., Rosino L., 1982, A&A, 116, 35
Barkat Z., Rakavy G., Sack N., 1967, Phys. Rev. Lett., 18, 379
Benetti S., 1992, PhD thesis, University of Padua and Italian National Institute for Astronomy
Benetti S. et al., 2014, MNRAS, 441, 289
Benetti S. et al., 2016, MNRAS, 456, 3296
Bessell M., Bloxham G., Schmidt B., Keller S., Tisserand P., Francis P., 2011, PASP, 123, 789
Bishop C., 2006, Pattern Recognition and Machine Learning. Springer, New York
Blanton M. R., Roweis S., 2007, AJ, 133, 734
Blinnikov S. I., Bartunov O. S., 1993, A&A, 273, 106
Bose S. et al., 2015, ApJ, 806, 160
Botticella M. T. et al., 2010, ApJ, 717, L52
Brown T. M. et al., 2013, PASP, 125, 1031
Campbell H. et al., 2014, The Astronomer's Telegram, 5912
Cappellaro E., Danziger I. J., Turatto M., 1995, MNRAS, 277, 106
Chatzopoulos E., Wheeler J. C., Vinko J., 2012, ApJ, 746, 121
Chatzopoulos E., Wheeler J. C., Vinko J., Horvath Z. L., Nagy A., 2013, ApJ, 773, 76
Chen T.-W. et al., 2015, MNRAS, 452, 1567
Chevalier R. A., Irwin C. M., 2011, ApJ, 729, L6
Childress M. J., Vogt F. P. A., Nielsen J., Sharp R. G., 2014, Ap&SS, 349, 617
Chugai N. N., 1985, Soviet Astronomy Letters, 11, 148
Chugai N. N., Chevalier R. A., Utrobin V. P., 2007, ApJ, 662, 1136
de Jaeger T. et al., 2017, MNRAS, 472, 4233
Dessart L., Hillier D. J., 2005, A&A, 437, 667
Dexter J., Kasen D., 2013, ApJ, 772, 30
Dopita M. et al., 2010, Ap&SS, 327, 245
Drake A. J. et al., 2009, ApJ, 696, 870
Elmhamdi A. et al., 2003, MNRAS, 338, 939
Faran T. et al., 2014, MNRAS, 445, 554
Fassia A. et al., 2001, MNRAS, 325, 907
Fesen R. A. et al., 1999, AJ, 117, 725
Fraley G. S., 1968, Ap&SS, 2, 96
Fraser M. et al., 2015, The Astronomer's Telegram, 7209
Freudling W., Romaniello M., Bramich D. M., Ballester P., Forchi V., García-Dabló C. E., Moehler S., Neeser M. J., 2013, A&A, 559, A96
Gal-Yam A., 2012, Science, 337, 927
Gal-Yam A. et al., 2007, ApJ, 656, 372
Gal-Yam A. et al., 2014, Nature, 509, 471
Galbany L. et al., 2016, AJ, 151, 33
Gall E. E. E. et al., 2015, A&A, 582, A3
Gezari S. et al., 2009, ApJ, 690, 1313
Gutiérrez C. P. et al., 2017a, ApJ, 850, 89
Gutiérrez C. P. et al., 2017b, ApJ, 850, 90
Hoflich P., 1991, A&A, 246, 481
Hogg D. W., Baldry I. K., Blanton M. R., Eisenstein D. J., 2002, preprint (arXiv:astro-ph/0210394)
Huber M. et al., 2015, The Astronomer's Telegram, 7153
Inserra C., Smartt S. J., 2014, ApJ, 796, 87
Inserra C. et al., 2011, MNRAS, 417, 261
Inserra C. et al., 2012a, MNRAS, 422, 1122
Inserra C., Baron E., Turatto M., 2012b, MNRAS, 422, 1178
Inserra C. et al., 2013a, A&A, 555, A142
Inserra C. et al., 2013b, ApJ, 770, 128
Inserra C. et al., 2015, ApJ, 799, L2
Inserra C. et al., 2016a, MNRAS, 459, 2721
Inserra C., Bulla M., Sim S. A., Smartt S. J., 2016b, ApJ, 831, 79
Inserra C., Prajs S., Gutierrez C. P., Smith C. A. M., Sullivan M., 2017a, preprint (arXiv:1711.03787)
Inserra C. et al., 2017b, preprint (arXiv:1710.09585)
Inserra C. et al., 2017c, MNRAS, 468, 4642
Ivezic Z., Connolly A. J., VanderPlas J. T., Gray A., 2014, Statistics, Data Mining, and Machine Learning in Astronomy: A Practical Python Guide for the Analysis of Survey Data. Princeton University Press, Princeton, NJ
Janka H.-T., 2012, Annual Review of Nuclear and Particle Science, 62, 407
Kangas T. et al., 2016, MNRAS, 456, 323
Kasen D., Bildsten L., 2010, ApJ, 717, 245
Keller S., Bessell M., Schmidt B., Francis P., 2007, in Sterken C., ed., ASP Conf. Ser. Vol. 364, The Future of Photometric, Spectrophotometric and Polarimetric Standardization. Astron. Soc. Pac., San Francisco, p. 177
Kim A., Goobar A., Perlmutter S., 1996, PASP, 108, 190
Kim A. G. et al., 2013, ApJ, 766, 84
Kozma C., Fransson C., 1998, ApJ, 497, 431
Krühler T. et al., 2015, A&A, 581, A125
Lantz B. et al., 2004, Proc. SPIE, 5249, 146
Leloudas G. et al., 2015a, MNRAS, 449, 917
Leloudas G. et al., 2015b, ApJ, 815, L10
Leloudas G. et al., 2017, ApJ, 837, L14
Li W. et al., 2011, MNRAS, 412, 1441
Lunnan R. et al., 2014, ApJ, 787, 138

Lunnan R. et al., 2016, ApJ, 831, 144
Magnier E. A. et al., 2013, ApJS, 205, 20
Maguire K. et al., 2010, MNRAS, 404, 981
Mazzali P. A., Sullivan M., Pian E., Greiner J., Kann D. A., 2016, MNRAS, 458, 3455
Miller A. A. et al., 2009, ApJ, 690, 1303
Moriya T. J., Yoon S.-C., Gräfener G., Blinnikov S. I., 2017, MNRAS, 469, L108
Morozova V., Piro A. L., Valenti S., 2017, ApJ, 838, 28
Nicholl M. et al., 2014, MNRAS, 444, 2096
Nicholl M. et al., 2015, MNRAS, 452, 3869
Ofek E. O. et al., 2007, ApJ, 659, L13
Papadopoulos A. et al., 2015, MNRAS, 449, 1215
Pastorello A. et al., 2010, ApJ, 724, L16
Pastorello A. et al., 2013, ApJ, 767, 1
Pastorello A. et al., 2015, MNRAS, 449, 1954
Patat F., Romaniello M., 2006, PASP, 118, 146
Patat F. et al., 2001, ApJ, 555, 900
Pignata G. et al., 2004, MNRAS, 355, 178
Polshaw J. et al., 2016, A&A, 588, A1
Poole T. S. et al., 2008, MNRAS, 383, 627
Pozzo M., Meikle W. P. S., Fassia A., Geballe T., Lundqvist P., Chugai N. N., Sollerman J., 2004, MNRAS, 352, 457
Prajs S. et al., 2017, MNRAS, 464, 3568
Pritchard T. A. et al., 2012, ApJ, 750, 128
Quimby R. M., Aldering G., Wheeler J. C., Höflich P., Akerlof C. W., Rykoff E. S., 2007, ApJ, 668, L99
Quimby R. M. et al., 2011, Nature, 474, 487
Quimby R. M., Yuan F., Akerlof C., Wheeler J. C., 2013, MNRAS, 431, 912
Rasmussen C. E., Williams C. K. I., 2006, Gaussian Processes for Machine Learning. MIT Press, Cambridge, MA
Sanders N. E. et al., 2015, ApJ, 799, 208
Scalzo R., Yuan F., Childress M., Tucker B., Schmidt B., 2013, The Astronomer's Telegram, 5480
Scalzo R. et al., 2014a, MNRAS, 440, 1498
Scalzo R. et al., 2014b, Central Bureau Electronic Telegrams, 3836
Schlafly E. F., Finkbeiner D. P., 2011, ApJ, 737, 103
Schlafly E. F. et al., 2012, ApJ, 756, 158
Schulze S. et al., 2018, MNRAS, 473, 1258
Smartt S. J., 2009, ARA&A, 47, 63
Smartt S. J., 2015, PASA, 32, e016
Smartt S. J. et al., 2015, A&A, 579, A40
Smartt S. J. et al., 2016, MNRAS, 462, 4094
Smith N., 2014, ARA&A, 52, 487
Smith N., McCray R., 2007, ApJ, 671, L17
Smith N., Owocki S. P., 2006, ApJ, 645, L45
Smith N., Humphreys R. M., Davidson K., Gehrz R. D., Schuster M. T., Krautter J., 2001, AJ, 121, 1111
Smith N. et al., 2007, ApJ, 666, 1116
Smith N. et al., 2015, MNRAS, 449, 1876
Steele I. A. et al., 2004, Proc. SPIE, 5489, 679
Stritzinger M. et al., 2002, AJ, 124, 2100
Tomasella L. et al., 2013, MNRAS, 434, 1636
Tonry J. L. et al., 2012, ApJ, 750, 99
Turatto M. et al., 2000, ApJ, 534, L57
Udalski A., Szymański M. K., Szymański G., 2015, AcA, 65, 1
Umeda H., Nomoto K., 2008, ApJ, 673, 1014
Uomoto A., Kirshner R. P., 1986, ApJ, 308, 685
Valenti S. et al., 2014, MNRAS, 438, L101
Valenti S. et al., 2015, MNRAS, 448, 2608
Valenti S. et al., 2016, MNRAS, 459, 3939
Wang L., Wheeler J. C., 2008, ARA&A, 46, 433
Wang L., Howell D. A., Höflich P., Wheeler J. C., 2001, ApJ, 550, 1030
Wang S. Q., Wang L. J., Dai Z. G., Wu X. F., 2015, ApJ, 799, 107
Woosley S. E., Weaver T. A., 1995, ApJS, 101, 181
Woosley S. E., Blinnikov S., Heger A., 2007, Nature, 450, 390
Xu Y., McCray R., Oliva E., Randich S., 1992, ApJ, 386, 181
Yan L. et al., 2015, ApJ, 814, 108
Yan L. et al., 2017, ApJ, 840, 57
Yaron O., Gal-Yam A., 2012, PASP, 124, 668
Yaron O. et al., 2017, Nature Physics, 13, 510

APPENDIX A: OBSERVATIONS AND DATA REDUCTION

Both objects were immediately selected by PESSTO as follow-up science targets and a combination of optical, NIR and UV photometric monitoring was carried out. The epochs of all the data, as well as the telescopes and instruments used, are listed in Appendix C.

All images were reduced (trimmed, bias subtracted and flat-fielded) by the SMT, PSST, Las Cumbres Observatory (LCO; Brown et al. 2013), Liverpool Telescope (LT; Steele et al. 2004), CRTS and PESSTO pipelines. Photometric zero-points and colour terms were computed using observations of standard fields (*U*, *B*, *V*, *R*, *I* in Vega and *g*, *r*, *i*, *z* in the AB system). We then calibrated the magnitudes of local stellar sequences shown in Appendix D. The average magnitudes of the local-sequence stars were used to calibrate the photometric zero-points in non-photometric nights. The NIR *J*, *H*, *K* photometry was carried out on SOFI on the NTT and the data were again reduced as discussed in Smartt et al. (2015). Magnitudes were calibrated to the Two-Micron All-Sky Survey (2MASS) system using local-sequence stars. The magnitudes of the SNe, obtained through a PSF fitting technique using standard procedures in IRAF,[8] were measured on the final images. The uncertainties reported in Tables C1, C2 and C3 in Appendix C were estimated by combining in quadrature the errors of photometric calibration and those on the instrumental magnitudes. When the objects were not detected, limiting magnitudes were estimated by placing artificial stars of different magnitudes at the expected SN positions. When necessary (i.e. after 170 d for SN2103hx and 100 d for PS15br), we applied a template subtraction technique (through the HOTPANTS[9] package based on the algorithm presented in Alard 2000). The instruments used to obtain the templates were NTT for SN2103hx and PSST for PS15br. The same frames were used to measure the host magnitudes and to host NIR limit magnitudes (see Sections 2.1 and 2.2).

Differences between passbands were taken into account by applying a passband correction (*P*-correction) using the SuperNova Algorithm for *P*-correction (SNAP) in the S3 package (see Appendix B for further details). This *P*-correction is similar to the *S*-correction (Stritzinger et al. 2002; Pignata et al. 2004).

Ultraviolet (*uvw*2, *uvm*2, *uvw*1; see Poole et al. 2008) observations, obtained by UVOT on board the *Swift* satellite (P.I. Margutti for SN2103hx and Inserra for PS15br) were reduced using NASA's High Energy Astrophysics Science Archive Research Center (HEASARC) software. We analysed these publicly available data independently. *Swift u*, *b*, *v* aperture magnitudes were transformed to the Johnson system by applying a shift after comparison with optical ground-based data taken close in time (see Inserra et al. 2011; Pastorello et al. 2013, for further details in the procedure).

Host-galaxy photometry was carried out through aperture photometry within the IRAF DAOPHOT package, and we used the same aperture size to measure the flux of local secondary standards in the

[8] The Image Reduction and Analysis Facility is distributed by the National Optical Astronomy Observatories, which are operated by the Association of Universities for Research in Astronomy, Inc, under contract to the National Science Foundation.
[9] http://www.astro.washington.edu/users/becker/hotpants.html

field. The *griz* photometry was calibrated against Pan-STARRS1 sequence stars, or local secondary stars, and converted to the SDSS photometric system; while JHK was calibrated against the 2MASS catalogue.

The journal of spectroscopic observations is listed in Table C7. The majority of the follow-up spectra were taken with PESSTO and the NTT. Integral field spectra were also taken with the ANU 2.3-m telescope + the Wide Field Spectrograph (WiFeS; Dopita et al. 2010) at Siding Spring Observatory in New South Wales, Australia. A final spectrum of PS15br was taken with the SuperNova Integral Field Spectrograph (SNIFS; Lantz et al. 2004) at the 2.2-m University of Hawaii Telescope. A series of spectra of SN2103hx was taken with the VLT+FORS2 in the second season of observations, and combined together into one deep late-time spectrum. These FORS2 exposures had a total of 11 × 1230 s and 1 × 1800 s and were taken on the nights of 2014 October 22–24 through the service mode on the VLT (giving an on-sky total exposure time of 4 h 15 min 30 s). However, two spectra of PS15br were taken with the VLT+XShooter in service mode. We used the custom-made pipeline described in Krühler et al. (2015), which takes the ESO pipeline produced two-dimensional spectral products (from REFLEX; Freudling et al. 2013) and uses optimal extraction with a Moffat profile fit. This pipeline produced flux-calibrated spectra with rebinned dispersions of 0.4 Å pix^{-1} in the UVB+VIS arms and 0.6 Å pix^{-1} in the NIR arm. The NTT spectral data were reduced using the PESSTO pipeline (Smartt et al. 2015), while the VLT+FORS2 spectra were reduced in the REFLEX environment (Freudling et al. 2013) and the SNIFS spectrum using standard IRAF procedures as described in Smartt et al. (2016). Optimal extraction of the spectra was adopted to improve the final S/N ratio. Wavelength calibration was performed using spectra of comparison lamps acquired with the same configurations as the SN observations. Atmospheric extinction correction was based on tabulated extinction coefficients for each telescope site. The WiFeS spectra were reduced with the PYWIFES[10] package (Childress et al. 2014) to produce data cubes, from which the final spectra were obtained using a PSF weighted extraction routine. Flux calibration was performed using spectrophotometric standard stars observed on the same nights with the same set-up as the SLSNe. The flux calibration was checked by comparison with the photometry, integrating the spectral flux transmitted by standard *griz* filters and adjusted by a multiplicative factor when necessary. The resulting flux calibration is accurate to within 0.1–0.2 mag.

All reduced spectra (and calibrated NIR images), taken at the NTT before 2014 April 30, are available from the ESO Science Archive Facility as PESSTO SSDR2 and details of data access are provided on the PESSTO web site.[11] Data taken after this date are part of the SSDR3. All spectra will also be available through WISeREP[12] (Yaron & Gal-Yam 2012).

APPENDIX B: S3 PACKAGE

The S3 package is a Python suite publicly available at https://github.com/cinserra and accepts fits, txt, dat and ascii files as input. It contains the following programs.

[10] http://www.mso.anu.edu.au/pywifes/
[11] www.pessto.org
[12] http://wiserep.weizmann.ac.il/home

B1 snake

The SuperNova Algorithm for *K*-correction Evaluation (SNAKE) and its light version developed to handle multiple input files in a less interactive fashion (SNAKELOOP) allow us to evaluate the *K*-correction from the observed passband (*P*) to the rest-frame, desired passband (*R*) according to the formula defined in Hogg et al. (2002); Blanton & Roweis (2007):

$$K_{\rm PR} = -2.5\log\left(\frac{1}{1+z}\right) - 2.5\log \times \left\{\frac{\int {\rm d}\lambda_{\rm o}\ \lambda_{\rm o}\ L_{\lambda}[\lambda_{\rm o}/(1+z)]P(\lambda_{\rm o})\int {\rm d}\lambda_{\rm e}\ \lambda_{\rm e}\ g^{R}_{\lambda}(\lambda_{\rm e})\ R(\lambda_{\rm e})}{\int {\rm d}\lambda_{\rm o}\ \lambda_{\rm o}\ g^{P}_{\lambda}(\lambda_{\rm o})P(\lambda_{\rm o})\int {\rm d}\lambda_{\rm e}\ \lambda_{\rm e}\ L_{\lambda}(\lambda_{\rm e})R(\lambda_{\rm e})}\right\}. \quad \text{(B1)}$$

Here, $P(\lambda)$ and $R(\lambda)$ are the filter response per unit photon, $g^{\rm passband}_{\lambda}$ are the flux densities per unit wavelength for the standard source for P and R, $\lambda_{\rm o}$ refers to the observer frame and $\lambda_{\rm e}$ to the rest frame. We note that the S3 package uses flux and not density flux, so the zero-points are also treated accordingly. GALEX FUV and NUV; UVOT *uvw*2, *uvm*2, *uvw*1; Johnson *UBVRI*; Sloan *u*, *g*, *r*, *i*, *z*; 2MASS *J*, *H*, *K*; Euclid NIR *Y*, *J*, *H* (Inserra et al. 2017b) and 4000 and 5200 Å passbands (created for the use of SLSNe as cosmological probes in Inserra & Smartt 2014) are recognized by the program and the cross *K*-correction (which is when the observed and rest-frame filter shapes are the most similar) is suggested. When more than 50 Å of one of the two filters chosen are not covered by the observer frame or rest-frame spectrum, the program allows the user to combine the spectrum with the best blackbody fit to the data. The output of the program is the *K*-correction ($K_{\rm PR}$) and it is related to the apparent and absolute magnitude as follows:

$$M_{\rm R} = m_{\rm P} - (5\log D_{\rm L} + 25) - A_P - K_{\rm PR}. \quad \text{(B2)}$$

Here, $M_{\rm R}$ is the absolute magnitude in the rest-frame filter, $m_{\rm P}$ is the apparent magnitude in the observed filter, $D_{\rm L}$ is the distance luminosity of the source and $A_{\rm P}$ is the foreground reddening extinction towards the source in the observed band. Assuming as a first approximation that the terms are uncorrelated and evaluating the single term errors as their variance, the overall error on the *K*-correction is a root mean square:

$$\sigma_K = \sqrt{\frac{\sigma_z^2 + \sigma^2_{{\rm ZP}_{\lambda_{\rm o}}} + \sigma^2_{{\rm ZP}_{\lambda_{\rm e}}} + \sigma^2_{\rm BB}}{N}}. \quad \text{(B3)}$$

Here, σ_z is the error on the redshift, which is set by default to be ± 0.005 and can be changed by the user; $\sigma_{ZP_{\lambda}}$ are the errors on the zero-points for the observed (o) and rest-frame (e) filters evaluated from the average of all the differences between the zero-points of the standard passbands (in the Vega and AB system) and those of the filters used by the telescopes listed in SNAP (see Section B2); $\sigma_{\rm BB}$ is the error on the assumption that a blackbody can be used to measure the wavelength uncovered by the spectrum for the filter chosen; N is the number of errors considered. Two other errors – related to the spectra template used when a spectrum of the object for the same, or very close in time, epoch of the photometry are not available – should be considered. However, the program does not handle this as they are highly dependent to the nature and the evolutionary phase of the object, for which the *K*-correction is needed.

In order to test the program reliability we compared our results with those published by Kim, Goobar & Perlmutter (1996), finding similar values. A previous, beta version, based on IRAF and STDAS

was used to calculate *K*-corrections in Inserra & Smartt (2014); Inserra et al. (2015), while this version has been used by Gall et al. (2015) and Polshaw et al. (2016). Furthermore, the program can also evaluate the *K*-correction when reddening is also applied and hence it can directly evaluate the term $-(A_{\rm P} + K_{\rm PR})$ of equation B2. However, this is not the correct way and the additional errors related to the assumed reddening and reddening law are not taken into account.

B2 snap

SNAP evaluates a *P*-correction given by

$$P_\lambda = F_\lambda \times QE_\lambda, \tag{B4}$$

where F_λ is the filter transmission function and QE_λ is the quantum efficiency of the detector. In contrast with the *S*-correction, the program does not take into account the lens throughput because, despite the use of a few materials, they are relatively flat across the optical range. However, this might cause some problems at wavelengths bluer than 3400 Å (i.e. affecting the *U* and *u* passbands). The atmospheric transmission profile is also ignored as SN magnitudes are usually evaluated through sequence stars calibrated with Sloan stars (and hence such correction is already taken into account at this level) or with Landolt stars and subsequent use of programs that apply such correction. We tested a few mirror reflectivity functions and found small dissimilarities between them, quantifiable in magnitude differences smaller or comparable with the usual photometric errors; hence we decided not to include such additional terms. Then, P_λ allows us to correct the apparent magnitude of a given telescope to that of the standard passband system as follows:

$$m_P = m_F - P_\lambda. \tag{B5}$$

Here, m_P is the apparent magnitude with the standard passbands (Johnson *U*, *B*, *V*, *R*, *I* or Sloan *u*, *g*, *r*, *i*, *z*) and m_F is the one measured with photometry at a given telescope. Like SNAKE, SNAP also evaluates the errors of the *P*-correction in the same way as equation B3 but without the redshift term and with the rest-frame filter considered as the error on the zero-point in flux of the standard passband.

We retrieved the information needed for the *P*-correction from various sources: the NTT (ESO web site), La Silla-Quest (LSQ; Baltay et al. 2007, and D. Rabinowitz, private communication), SkyMapper (SMT; Bessell et al. 2011, M. Renault and R. Scalzo, private communications), the Liverpool Telescope (LT web site), the Las Cumbres Observatory Global Network (LCOGT; S. Valenti, private communication), the Optical Gravitational Lensing Experiment IV (OGLE-IV; Udalski, Szymański & Szymański 2015, and L. Wyrzykowski private communication), the North Optical Telescope (NOT; NOT web site), the Pan-STARSS1 survey (PS1; Tonry et al. 2012, and K. W. Smith, private communication), the Telescopio Nazionale Galileo (TNG; TNG web site) and the Copernico Telescope at Cima Ekar in Asiago (EKAR; S. Benetti, private communication).

B3 sms

The Synthetic Magnitudes from Spectra (SMS) program is just a Python version of the STSDAS/HST IRAF tool CALCPHOT. It evaluates the flux in a given passband and converts it into magnitudes (AB or Vega system) for the same filter list used by SNAKE. Like SNAKE, it evaluates the errors in the same fashion as SNAKE but without the terms about the redshift and the rest-frame filter.

APPENDIX C: TABLES

Table C1. *U*, *B*, *V*, *g*, *r*, *i*, *J*, *H*, *K* magnitudes of SN2103hx and assigned errors in brackets. Phase is with respect to the *r*-band maximum.

Date (yy/mm/dd)	MJD	Phase (d)	*U*	*B*	*V*	*g*	*r*	*i*	Inst.
13/10/01	56566.61	− 104.32	–	–	–	>20.86	>20.68	–	SMT
13/10/08	56573.58	− 98.16	–	–	–	–	>20.71	–	SMT
13/10/19	56584.62	− 88.39	–	–	–	>18.97	>19.24	–	SMT
13/10/28	56593.63	− 80.41	–	–	–	>19.89	>19.65	–	SMT
13/11/01	56597.64	− 76.87	–	–	–	>20.19	>19.98	–	SMT
13/11/06	56602.60	− 72.48	–	–	–	>20.24	>20.02	–	SMT
13/11/10	56606.64	− 68.90	–	–	–	>19.63	>19.64	–	SMT
13/11/15	56611.65	− 64.47	–	–	–	>19.20	–	–	SMT
13/11/20	56616.62	− 60.07	–	–	–	>18.59	>18.68	–	SMT
13/11/25	56621.60	− 55.66	–	–	–	>20.03	>19.95	–	SMT
13/11/30	56626.58	− 51.26	–	–	–	>19.94	>19.91	–	SMT
13/12/01	56627.55	− 50.40	–	–	–	>20.30	>19.99	–	SMT
13/12/06	56632.55	− 45.97	–	–	–	–	>20.28	–	SMT
13/12/27	56653.51	− 27.42	–	–	–	17.86 (0.04)	18.14 (0.06)	–	SMT
13/12/31	56657.55	− 23.85	–	–	–	17.50 (0.06)	17.83 (0.08)	–	SMT
14/01/04	56661.48	− 20.37	–	–	–	17.33 (0.02)	17.61 (0.06)	–	SMT
14/01/04	56661.49	− 20.36	–	–	–	17.32 (0.02)	17.62 (0.06)	–	SMT
14/01/05	56662.50	− 19.47	–	–	–	17.27 (0.04)	17.52 (0.05)	–	SMT
14/01/07	56664.49	− 17.71	–	–	–	17.09 (0.26)	17.47 (0.08)	–	SMT
14/01/07	56664.50	− 17.70	–	–	–	17.20 (0.05)	17.43 (0.08)	–	SMT
14/01/25	56682.47	− 1.80	–	–	–	16.88 (0.04)	17.07 (0.08)	–	SMT
14/01/26	56683.51	− 0.88	–	–	–	16.89 (0.03)	17.09 (0.08)	–	SMT
14/01/26	56683.52	− 0.87	–	–	–	16.88 (0.03)	17.06 (0.09)	–	SMT
14/01/27	56684.50	0.00	–	–	–	16.86 (0.27)	17.12 (0.13)	–	SMT
14/01/28	56685.49	0.88	–	–	–	16.89 (0.05)	17.12 (0.11)	–	SMT
14/01/29	56686.48	1.75	–	–	–	16.94 (0.04)	17.06 (0.10)	–	SMT
14/01/29	56686.49	1.76	–	–	–	16.95 (0.05)	17.13 (0.11)	–	SMT
14/01/30	56687.48	2.64	–	–	–	16.95 (0.06)	17.09 (0.09)	–	SMT
14/01/31	56688.47	3.51	–	–	–	–	17.14 (0.11)	–	SMT
14/02/06	56694.49	8.84	–	–	–	17.06 (0.05)	17.16 (0.09)	–	SMT
14/02/19	56708.03	20.82	–	–	16.76 (0.02)	–	–	–	NTT
14/02/20	56709.02	21.70	–	–	16.83 (0.01)	–	–	–	NTT
14/02/21	56709.88	22.56	17.08 (0.09)	17.67 (0.09)	16.89 (0.12)	–	–	–	SWIFT
14/02/21	56710.02	22.58	–	–	16.86 (0.02)	–	–	–	NTT
14/02/21	56711.02	23.47	–	–	16.87 (0.02)	–	–	–	NTT
14/02/24	56712.82	25.17	17.35 (0.08)	17.74 (0.10)	17.04 (0.19)	–	–	–	SWIFT
14/02/27	56715.36	27.43	17.48 (0.08)	17.91 (0.10)	17.21 (0.31)	–	–	–	SWIFT
14/02/28	56717.04	28.80	–	–	17.06 (0.02)	–	–	–	NTT
14/03/03	56719.16	30.81	17.73 (0.08)	17.78 (0.10)	17.15 (0.14)	–	–	–	SWIFT
14/03/05	56721.17	32.59	17.74 (0.09)	17.92 (0.10)	17.22 (0.14)	–	–	–	SWIFT
14/03/08	56724.56	35.61	17.96 (0.09)	18.07 (0.10)	17.29 (0.12)	–	–	–	SWIFT
14/03/08	56725.02	35.86	–	–	17.28 (0.02)	–	–	–	NTT
14/03/09	56726.02	36.74	–	–	17.40 (0.02)	–	–	–	NTT
14/03/10	56727.02	37.62	–	–	17.52 (0.02)	–	–	–	NTT
14/07/06	56844.40	141.50	–	22.30 (0.15)	21.80 (0.10)	22.32 (0.10)	21.80 (0.10)	20.70 (0.10)	LCO
14/07/10	56848.40	145.04	–	22.48 (0.15)	22.05 (0.10)	22.49 (0.10)	21.88 (0.10)	20.83 (0.10)	LCO
14/07/13	56851.72	147.98	–	–	–	–	>21.50	–	LCO
14/07/31	56869.68	163.88	–	–	–	>21.29	>20.94	–	SMT
14/08/15	56885.23	177.64	–	–	–	–	21.74 (0.09)	–	NTT
14/08/25	56895.17	186.43	–	–	–	–	21.87[a] (0.06)	21.50 (0.05)	NTT
14/09/21	56922.10	210.27	–	–	23.26 (0.19)	–	22.34[a] (0.06)	–	NTT
14/09/23	56924.15	212.08	–	–	–	23.72 (0.10)	22.54 (0.14)	21.80 (0.09)	NTT
14/10/21	56952.15	236.86	–	–	–	24.75 (0.17)	23.23 (0.24)	22.35 (0.14)	NTT
14/12/22	56975.11	257.18	–	–	–	24.96 (0.26)	23.68 (0.29)	22.80 (0.19)	NTT
15/02/18	57072.04	344.48	–	–	–	–	–	>24.00	NTT
Host A									
15/01/20	57043.09	318.75	–	–	–	–	23.26 (0.16)	–	NTT
15/12/10	57367.12	606.77	–	–	–	24.43 (0.16)	23.20 (0.16)	21.82 (0.16)	NTT
Host B									
16/02/01	57420.08	653.85	–	–	–	24.71 (0.38)	24.55 (0.35)	23.54 (0.32)	Magellan

Table C1 *– continued*

Date (yy/mm/dd)	MJD	Phase (d)	*J*	*H*	*K*	Telescope
14/11/23	56985.12	266.03	22.21 (0.18)	>22.50	21.48 (0.12)	NTT
14/12/20	57012.10	289.91	–	–	22.10 (0.42)	NTT
14/12/29	57021.02	297.90	–	–	>22.18	NTT
Host A						
15/12/17	57374.12	613.00	>23.10	>23.00	>23.20	NTT

Note. [a] *r* in the AB magnitude system from the *R*-band filter converted through SNAP, as only these two observations were carried out with the *R* filter.

Table C2. *g*, *r*, *i*, *z* magnitudes of PS15br and assigned errors in brackets. Phase is with respect to the *r*-band maximum.

Date (yy/mm/dd)	MJD	Phase (d)	*g*	*r*	*i*	*z*	Inst.
15/01/16	57038.41	−46.15	–	>20.6	–	–	CSS
15/02/16	57069.43	−17.99	–	18.95[a] (0.07)	–	–	PSST
15/02/17	57070.43	−16.99	–	18.86[a] (0.07)	–	–	PSST
15/02/26	57079.48	−8.87	–	18.33 (0.07)	–	–	CSS
15/03/10	57091.52	2.06	–	18.24 (0.07)	–	–	CSS
15/03/11	57093.01	3.41	18.16 (0.01)	18.25 (0.01)	18.24 (0.01)	18.40 (0.02)	LT
15/03/14	57095.94	6.07	18.17 (0.01)	18.21 (0.01)	18.24 (0.02)	18.40 (0.03)	LT
15/03/19	57100.84	10.52	18.34 (0.07)	18.25 (0.07)	18.32 (0.07)	–	LCO
15/03/19	57100.91	10.59	18.31 (0.07)	18.29 (0.10)	18.33 (0.07)	–	LCO
15/03/21	57102.52	12.05	–	18.36 (0.07)	–	–	CSS
15/03/23	57104.57	13.91	18.45 (0.07)	18.38 (0.07)	18.37 (0.07)	–	LCO
15/03/24	57105.50	14.75	–	18.41[a] (0.07)	–	–	PSST
15/03/25	57106.51	15.67	–	18.44[a] (0.07)	–	–	PSST
15/03/27	57108.45	17.43	18.48 (0.07)	18.45 (0.08)	18.36 (0.07)	–	LCO
15/03/31	57112.90	21.47	18.57 (0.05)	18.40 (0.03)	18.36 (0.04)	18.45 (0.06)	LT
15/04/04	57117.03	25.22	18.58 (0.08)	18.42 (0.07)	18.40 (0.11)	–	LCO
15/04/07	57120.40	28.28	18.60 (0.09)	18.45 (0.08)	18.44 (0.11)	–	LCO
15/04/10	57121.52	29.29	–	18.52 (0.07)	–	–	CSS
15/04/10	57122.94	30.58	18.70 (0.01)	18.55 (0.02)	18.42 (0.01)	18.48 (0.06)	LT
15/04/11	57124.46	31.96	18.73 (0.08)	18.63 (0.08)	18.45 (0.11)	–	LCO
15/04/12	57124.94	32.40	18.77 (0.01)	18.61 (0.01)	18.46 (0.02)	18.50 (0.02)	LT
15/04/14	57126.94	34.21	18.78 (0.01)	18.61 (0.01)	18.48 (0.02)	18.48 (0.02)	LT
15/04/16	57128.44	35.58	–	18.66[a] (0.07)	–	–	PSST
15/04/16	57128.52	35.65	–	18.69 (0.07)	–	–	CSS
15/04/16	57128.99	36.07	18.96 (0.08)	–	–	–	LCO
15/04/17	57129.88	36.88	18.97 (0.09)	18.70 (0.08)	18.49 (0.11)	–	LCO
15/04/17	57129.93	36.93	18.95 (0.01)	18.66 (0.02)	18.50 (0.01)	18.49 (0.01)	LT
15/04/18	57130.42	37.37	–	18.67 (0.07)	–	–	PSST
15/04/20	57132.94	39.66	18.96 (0.02)	18.70 (0.01)	18.52 (0.01)	18.62 (0.02)	LT
15/04/22	57134.79	41.34	19.03 (0.09)	18.74 (0.08)	18.56 (0.11)		LCO
15/04/23	57135.95	42.39	19.06 (0.02)	18.74 (0.02)	18.48 (0.01)	18.53 (0.01)	LT
15/04/24	57136.52	42.91	–	18.71 (0.07)	–	–	CSS
15/04/25	57138.93	45.10	19.06 (0.02)	18.75 (0.02)	18.49 (0.02)	18.59 (0.02)	LT
15/04/26	57139.39	45.52	19.10 (0.10)	18.79 (0.07)	18.60 (0.08)	–	LCO
15/05/01	57144.29	49.96	19.21 (0.10)	18.79 (0.07)	18.58 (0.08)	–	LCO
15/05/02	57144.88	50.50	19.23 (0.06)	18.86 (0.07)	18.56 (0.03)	18.514 (0.03)	LT
15/05/04	57147.47	52.85	19.24 (0.10)	18.94 (0.07)	18.78 (0.08)	–	LCO
15/05/07	57149.52	54.71	–	18.92 (0.07)	–	–	CSS
15/05/08	57150.93	55.99	19.25 (0.02)	18.91 (0.01)	18.80 (0.03)	18.60 (0.02)	LT
15/05/10	57152.24	57.18	19.24 (0.10)	18.97 (0.07)	18.79 (0.08)	–	LCO
15/05/13	57155.52	60.16	–	18.97 (0.07)	–	–	CSS
15/05/14	57156.42	60.97	19.25 (0.10)	19.05 (0.07)	18.68 (0.08)	–	LCO
15/05/16	57158.86	63.19	19.23 (0.10)	19.05 (0.04)	18.74 (0.04)	18.71 (0.02)	LT
15/05/20	57162.87	66.83	19.25 (0.10)	19.05 (0.05)	18.72 (0.03)	18.76 (0.05)	LT
15/05/22	57164.52	68.33	–	19.10 (0.07)	–	–	CSS
15/05/24	57166.91	70.50	19.45 (0.03)	19.16 (0.03)	18.80 (0.02)	18.82 (0.02)	LT
15/06/02	57175.31	78.12	19.57 (0.15)	19.28 (0.15)	18.91 (0.12)	–	LCO
15/06/03	57176.97	79.63	19.56 (0.08)	19.31 (0.05)	18.90 (0.04)	19.03 (0.06)	LT
15/06/11	57184.27	86.26	19.83 (0.10)	19.39 (0.20)	19.10 (0.12)	–	LCO
15/06/12	57185.00	86.92	–	19.37 (0.20)	–	–	CSS

Table C2 – *continued*

Date (yy/mm/dd)	MJD	Phase (d)	*g*	*r*	*i*	*z*	Inst.
15/06/20	57193.37	94.52	–	–	19.15 (0.20)	–	LCO
15/06/30	57203.28	103.51	20.10 (0.20)	19.43 (0.15)	19.18 (0.10)	–	LCO
15/07/02	57205.27	105.32	20.30 (0.30)	19.75 (0.20)	19.28 (0.20)	–	LCO
15/12/08	57365.21	250.64			19.61 (0.08)		LT
15/12/13	57370.18	255.16	20.41 (0.06)	20.49 (0.07)		20.05 (0.07)	LT
15/12/18	57375.15	259.67	20.44 (0.10)	20.43 (0.10)	19.63 (0.11)	20.07 (0.11)	LT
16/01/17	57405.26	287.02	20.66 (0.10)	20.44 (0.09)	19.82 (0.11)	20.10 (0.15)	NTT
16/01/18	57406.04	287.73	20.52 (0.12)	20.49 (0.11)	19.83 (0.12)	20.13 (0.22)	LT
16/01/25	57413.10	294.12	20.55 (0.14)	20.45 (0.12)	19.88 (0.11)	20.11 (0.21)	LT
16/02/05	57424.25	304.27	20.56 (0.10)	20.51 (0.11)	19.90 (0.10)	20.19 (0.10)	NTT
16/03/08	57456.24	333.32	20.56 (0.09)	20.51 (0.10)	19.85 (0.15)	20.47 (0.10)	NTT
16/04/12	57491.11	365.00	20.91 (0.09)	20.74 (0.09)	19.86 (0.15)	20.54 (0.09)	NTT
Host							
10/05/01–14/10/01			22.39 (0.11)	22.18 (0.12)	21.70 (0.09)	22.15 (0.11)	PS1

Note. [a]*r* in the AB magnitude system from the *w*-band filter converted through SNAP.

Table C3. *U*, *B*, *V*, *J*, *H*, *K* magnitudes of PS15br and assigned errors in brackets. Phase is with respect to the *r*-band maximum.

Date (yy/mm/dd)	MJD	Phase (d)	*U*	*B*	*V*	Inst.
15/03/10	57092.07	2.56	–	–	18.00 (0.01)	NTT
15/03/11	57092.87	3.29	17.88 (0.10)	18.44 (0.10)	18.04 (0.13)	SWIFT
15/03/12	57094.23	4.52	–	–	17.95 (0.01)	NTT
15/03/13	57095.20	5.40	–	–	17.97 (0.02)	NTT
15/03/14	57095.96	6.09	17.95 (0.13)	18.48 (0.13)	18.05 (0.19)	SWIFT
15/03/19	57100.84	10.52	–	18.51 (0.10)	18.10 (0.07)	LCO
15/03/19	57100.91	10.58	–	18.63 (0.08)	18.15 (0.07)	LCO
15/03/20	57102.22	11.77	18.32 (0.11)	18.64 (0.12)	18.18 (0.21)	SWIFT
15/03/23	57104.57	13.91	–	18.67 (0.08)	18.21 (0.07)	LCO
15/03/23	57105.14	14.42	18.65 (0.15)	18.73 (0.19)	18.21 (0.21)	SWIFT
15/03/26	57107.93	16.96	18.80 (0.15)	18.83 (0.19)	18.30 (0.23)	SWIFT
15/03/27	57108.45	17.43	–	18.82 (0.08)	18.34 (0.07)	LCO
15/03/27	57109.30	18.20	–	–	18.35 (0.06)	NTT
15/03/28	57110.04	18.87	–	–	18.30 (0.01)	NTT
15/03/30	57112.15	20.79	19.02 (0.18)	19.01 (0.13)	18.38 (0.21)	SWIFT
15/04/04	57116.99	25.18	19.22 (0.18)	19.04 (0.18)	18.43 (0.21)	SWIFT
15/04/04	57117.03	25.22	–	19.05 (0.15)	18.44 (0.10)	LCO
15/04/07	57119.98	27.90	19.42 (0.18)	19.07 (0.18)	18.50 (0.21)	SWIFT
15/04/07	57120.40	28.28	–	19.08 (0.15)	18.49 (0.14)	LCO
15/04/11	57124.46	31.96	–	19.17 (0.11)	18.58 (0.09)	LCO
15/04/16	57128.99	36.07	–	19.19 (0.13)	18.76 (0.10)	LCO
15/04/17	57129.88	36.88	–	19.30 (0.11)	18.79 (0.11)	LCO
15/04/18	57130.81	37.73	–	19.45 (0.11)	18.80 (0.09)	LCO
15/04/22	57134.79	41.34	–	19.47 (0.20)	18.85 (0.11)	LCO
15/04/25	57138.13	44.37	–	–	18.84 (0.03)	NTT
15/04/26	57139.39	45.52	–	19.44 (0.12)	18.81 (0.10)	LCO
15/05/01	57144.29	49.96	–	19.43 (0.12)	18.84 (0.10)	LCO
15/05/04	57147.47	52.85	–	19.42 (0.12)	18.84 (0.10)	LCO
15/05/10	57152.24	57.18	–	19.59 (0.12)	18.86 (0.10)	LCO
15/05/14	57156.42	60.97	–	19.67 (0.20)	19.15 (0.10)	LCO
			J	*H*	*K*	Telescope
15/03/11	57093.22	3.60	17.80 (0.02)	17.48 (0.03)	17.27 (0.06)	NTT
15/04/16	57129.14	36.21	17.76 (0.01)	17.23 (0.01)	17.01 (0.02)	NTT
16/01/16	57404.25	286.10	19.06 (0.05)	18.95 (0.05)	17.61 (0.08)	NTT
16/02/06	57425.16	305.09	19.293 (0.12)	19.105 (0.10)	17.630 (0.08)	NTT
16/03/07	57455.22	332.40	19.098 (0.25)	19.239 (0.08)	17.537 (0.12)	NTT
16/04/13	57492.09	365.89	19.425 (0.12)	19.514 (0.18)	17.659 (0.08)	NTT

Table C4. *Swift*+UVOT *uvw*2, *uvm*2, *uvw*1 magnitudes of SN2103hx and PS15br and assigned errors in brackets. Phase is with respect to the *r*-band maximum.

Date (yy/mm/dd)	MJD	Phase* (d)	*uvw*2	*uvm*2	*uvw*1
			SN2103hx		
14/02/21	56709.88	22.56	17.67.10	17.44.08	17.17.09
14/02/24	56712.82	25.17	17.87.10	17.75.08	17.46.09
14/02/27	56715.36	27.43	18.10.12	18.05.16	17.63.09
14/03/03	56719.16	30.81	18.49.12	18.13.10	18.01.11
14/03/05	56721.17	32.59	18.58.13	18.38.11	18.07.13
14/03/08	56724.56	35.61	18.85.13	18.58.11	18.34.12
14/04/27	56774.90	80.35	–	>21.0	–
14/04/28	56775.03	80.47	–	–	>21.8
14/04/30	56777.36	82.54	>22.0	–	–
14/07/07	56845.79	143.37	>21.9	–	–
14/07/21	56859.07	155.17	–	–	>21.6
14/07/24	56862.46	158.19	–	>21.1	–
			PS15br		
15/03/11	57092.87	3.29	18.70 (0.11)	18.67 (0.17)	18.25 (0.11)
15/03/14	57095.96	6.09	19.01 (0.17)	18.87 (0.22)	18.50 (0.18)
15/03/20	57102.22	11.77	19.37 (0.14)	19.24 (0.19)	18.83 (0.15)
15/03/23	57105.14	14.42	19.57 (0.21)	19.44 (0.32)	18.85 (0.15)
15/03/26	57107.93	16.96	19.78 (0.18)	19.13 (0.19)	18.92 (0.16)
15/03/30	57112.15	20.79	20.06 (0.19)	19.77 (0.24)	19.29 (0.18)
15/04/04	57116.99	25.18	20.26 (0.30)	19.94 (0.26)	19.47 (0.24)
15/04/07	57119.98	27.90	20.39 (0.24)	20.03 (0.28)	19.62 (0.28)
15/11/11	57337.64	225.60	21.15 (0.23)	–	
15/11/15	57341.03	228.68	20.92 (0.24)	–	
16/01/21	57407.80	289.33	–	–	20.98 (0.38)
16/01/25	57412.04	293.18	21.03 (0.27)	21.04 (0.30)	20.65 (0.25)

Table C5. Magnitudes in *B*, *V*, *g*, *r*, *i* of the local-sequence stars in the field of SN2103hx.

Star	*B*	*V*	*g*	*r*	*i*
1	21.06 (0.09)	19.24 (0.05)	19.35 (0.03)	17.81 (0.03)	16.55 (0.02)
2	18.96 (0.06)	16.68 (0.02)	16.83 (0.02)	15.26 (0.03)	13.81 (0.02)
3	19.59 (0.07)	18.17 (0.03)	17.98 (0.02)	17.30 (0.02)	16.69 (0.02)
4	–	22.89 (0.09)	22.90 (0.08)	21.17 (0.08)	20.65 (0.05)
5	20.56 (0.08)	18.76 (0.05)	18.90 (0.04)	17.39 (0.05)	15.94 (0.02)
6	19.29 (0.07)	17.95 (0.06)	17.72 (0.03)	17.20 (0.03)	16.65 (0.03)
7	–	22.50 (0.09)	22.17 (0.06)	20.41 (0.05)	18.40 (0.04)
8	–	22.50 (0.08)	22.61 (0.09)	21.82 (0.08)	21.34 (0.06)
9	–	22.54 (0.08)	22.77 (0.09)	21.11 (0.07)	19.13 (0.04)
10	17.42 (0.05)	16.04 (0.02)	15.83 (0.02)	15.15 (0.02)	14.67 (0.03)
11	–	22.22 (0.08)	22.38 (0.08)	21.07 (0.07)	20.21 (0.05)
12	–	22.36 (0.08)	22.50 (0.09)	21.15 (0.07)	20.28 (0.05)

Table C6. Magnitudes in *B*, *V*, *g*, *r*, *i*, *z* of the local sequence stars in the field of PS15br.

Star	*B*	*V*	*g*	*r*	*i*	*z*
1	16.50 (0.02)	16.02 (0.02)	16.19 (0.01)	15.96 (0.01)	15.83 (0.02)	15.83 (0.01)
2	18.02 (0.02)	17.47 (0.02)	17.67 (0.01)	17.38 (0.01)	17.22 (0.01)	17.18 (0.01)
3	20.57 (0.05)	19.32 (0.03)	19.86 (0.02)	18.85 (0.01)	18.27 (0.01)	17.97 (0.01)
4	17.41 (0.02)	16.51 (0.02)	16.91 (0.01)	16.16 (0.01)	15.85 (0.01)	15.69 (0.01)
5	19.03 (0.03)	17.89 (0.02)	18.41 (0.01)	17.44 (0.01)	16.97 (0.01)	16.72 (0.01)
6	19.12 (0.03)	18.65 (0.03)	18.81 (0.02)	18.60 (0.01)	18.49 (0.01)	18.47 (0.01)
7	18.33 (0.03)	17.80 (0.02)	17.99 (0.01)	17.70 (0.01)	17.55 (0.01)	17.52 (0.01)
8	20.17 (0.05)	18.51 (0.03)	19.07 (0.02)	17.89 (0.01)	16.96 (0.01)	16.49 (0.01)
9	18.07 (0.02)	17.44 (0.02)	17.68 (0.01)	17.29 (0.01)	17.08 (0.01)	17.01 (0.01)
10	20.75 (0.05)	19.59 (0.05)	20.09 (0.02)	19.15 (0.01)	18.63 (0.01)	18.37 (0.01)
11	21.48 (0.06)	20.15 (0.05)	20.72 (0.03)	19.63 (0.02)	19.03 (0.02)	18.66 (0.01)

Table C7. Journal of spectroscopic observations. Phase is with respect to the *r*-band maximum. Range is with respect to the observed frame.

Date (yy/mm/dd)	MJD	Phase (d)	Range (Å)	Resolution (Å)	Instrumental configuration
			SN2103hx		
14/01/31	56688.43	3.49	3100–6900	1.5/2.5	ANU 2.3m+WiFeS+B300/R300
14/02/19	56708.03	20.82	3600–9300	18	NTT+EFOSC2+gm13
14/02/20	56709.02	21.70	3600–9300	18	NTT+EFOSC2+gm13
14/02/21	56710.02	22.58	6000–10 000	16	NTT+EFOSC2+gm16
14/02/22	56711.02	23.47	3300–7500	13	NTT+EFOSC2+gm11
14/02/24	56712.44	24.84	3400–6900	1.5/2.5	ANU 2.3m+WiFeS+B300/R300
14/02/28	56717.04	28.80	3300–10 000	13/16	NTT+EFOSC2+gm11/gm16
14/03/04	56720.42	31.93	3400–6900	1.5/2.5	ANU 2.3m+WiFeS+B300/R300
14/03/08	56725.03	35.87	6000–10 000	16	NTT+EFOSC2+gm16
14/03/09	56726.06	36.78	3300–10 000	13/16	NTT+EFOSC2+gm11/gm16
14/03/10	56727.02	37.62	3300–7500	13	NTT+EFOSC2+gm11
14/03/14	56730.39	40.79	3400–6900	1.5/2.5	ANU 2.3m+WiFeS+B300/R300
14/09/21	56922.10	210.27	6900–7700	18	NTT+EFOSC2+gm13
14/10/22	56953.07	237.67	4500–9300	11	VLT+FORS2+GRIS_300V
			PS15br		
15/03/10	57092.07	2.56	3600–9300	18	NTT+EFOSC2+gm13
15/03/12	57093.56	3.91	4100–6900	1.5/2.5	ANU 2.3m+WiFeS+B300/R300
15/03/12	57094.23	4.52	3300–7500	13	NTT+EFOSC2+gm11
15/03/13	57095.20	5.40	6000–10 000	16	NTT+EFOSC2+gm16
15/03/27	57109.30	18.20	3300–10 000	18	NTT+EFOSC2+gm13
15/03/28	57100.05	18.88	3600–9300	18	NTT+EFOSC2+gm13
15/04/12	57125.06	32.51	3600–9300	18	NTT+EFOSC2+gm13
15/04/25	57138.13	44.37	3600–9300	18	NTT+EFOSC2+gm13
15/06/29	57202.13	102.47	3600–9300	4.3/5.8	UH 2.2m+SNIFS+B/R
16/01/08	57396.24	278.82	3600–9300	18	NTT+EFOSC2+gm13
16/03/12	57460.26	336.98	2811–24 511	1.0/1.1/3.3	VLT+XSHOOTER+UV/OPT/NIR
16/04/09	57488.08	362.24	2811–24 511	1.0/1.1/3.3	VLT+XSHOOTER+UV/OPT/NIR
16/04/10	57489.09	363.16	3600–9300	18	NTT+EFOSC2+gm13

APPENDIX D: SEQUENCE STARS AND ADDITIONAL PLOTS

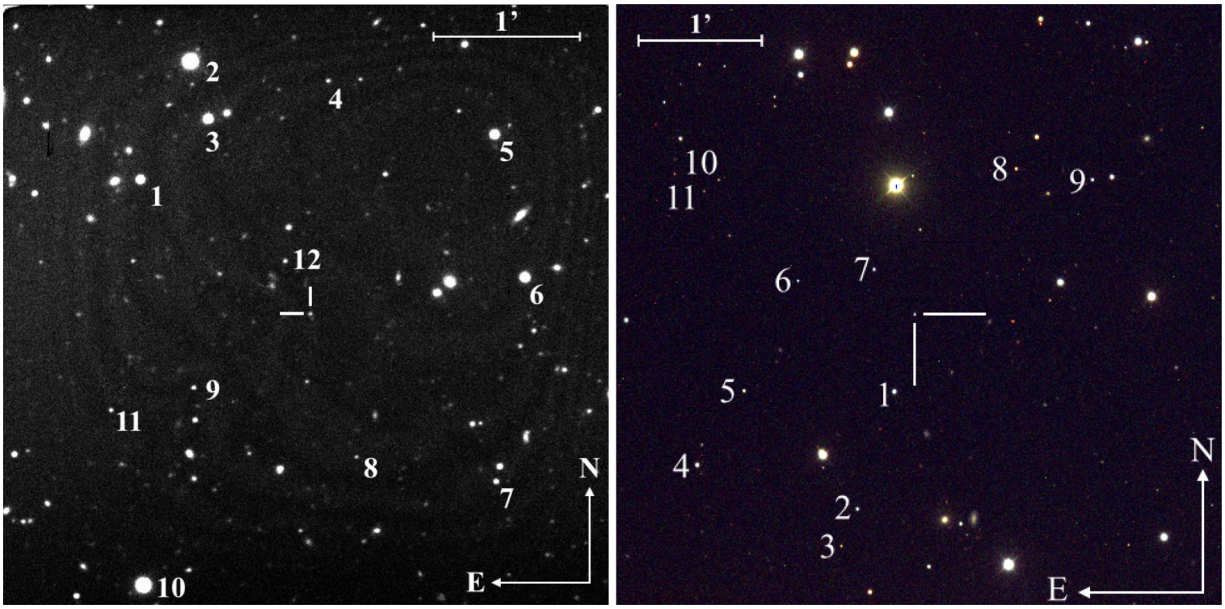

Figure D1. Left: NTT+EFOSC2+*r* image of SN2103hx. The SN position is indicated with cross white marks. The sequence of stars in the field used to calibrate the optical and NIR magnitudes of SN2103hx is indicated. Right: LT+IO+*g*/*r*/*i* image of PS15br (cross white marks). The sequence of stars in the field used to calibrate the optical and NIR magnitudes of PS15br is indicated.

[1]*Department of Physics and Astronomy, University of Southampton, Southampton, SO17 1BJ*
[2]*Astrophysics Research Centre, School of Mathematics and Physics, Queens University Belfast, Belfast BT7 1NN*
[3]*Max-Planck-Institut für Astrophysik, Karl-Schwarzschild-Str. 1, DE-85748 Garching-bei-München, Germany*
[4]*Dark Cosmology Centre, Niels Bohr Institute, University of Copenhagen, Juliane Maries vej 30, 2100 Copenhagen, Denmark*
[5]*Max-Planck-Institut für Extraterrestrische Physik, Giessenbachstraße 1, 85748, Garching, Germany*
[6]*Instituto de Astrofísica, Facultad de Física, Pontificia Universidad Católica de Chile, Vicuña Mackenna 4860, 7820436 Macul, Santiago, Chile*
[7]*Millennium Institute of Astrophysics, Vicuña Mackenna 4860, 7820436 Macul, Santiago, Chile*
[8]*Max-Planck Institut für Astrophysik, Karl-Schwarzschild-Str. 1, D-85748 Garching, Munich, Germany*
[9]*Harvard-Smithsonian Center for Astrophysics, 60 Garden Street, Cambridge, Massachusetts 02138, USA*
[10]*European Southern Observatory, Alonso de Córdova 3107, Casilla 19, Santiago, Chile*
[11]*Las Cumbres Observatory Global Telescope Network, 6740 Cortona Dr., Suite 102 Goleta, CA 93117, USA*
[12]*Department of Physics, University of California, Santa Barbara, CA 93106-9530, USA*
[13]*INAF, Osservatorio Astronomico di Padova, vicolo dell'Osservatorio 5, 35122, Padova, Italy*
[14]*INAF Osservatorio Astronomico di Capodimonte, Salita Moiariello 16, I-80131 Napoli, Italy*
[15]*Institute for Astronomy, University of Hawaii at Manoa,Honolulu, HI 96822, USA*
[16]*School of Physics, O'Brien Centre for Science North, University College Dublin, Belfield, Dublin 4, Ireland*
[17]*Department of Particle Physics and Astrophysics, Weizmann Institute of Science, Rehovot 7610001, Israel*
[18]*Research School of Astronomy and Astrophysics, Australian National University, Canberra, ACT 2611, Australia*
[19]*ARC Centre of Excellence for All-Sky Astrophysics (CAASTRO), The Australian National University, Canberra, ACT 2611, Australia*
[20]*Australian National University, Canberra, ACT 2611, Australia*
[21]*Department of Physics, University of California, Davis, CA 95616, USA*

This paper has been typeset from a TEX/LATEX file prepared by the author.